Fluidized Bed Hydrodynamics by means of Electrical Capacitance Tomography

A Thesis Submitted to the College of Graduate Studies and Research

in partial fulfilment of the requirements for the degree of

Master of Science

in the Department of Chemical & Biological Engineering

University of Saskatchewan

By

Mohammad Omer Choudhary

Permission for Use

The author has agreed that the Libraries of the University of Saskatchewan may make this thesis freely available for inspection. Moreover, the author has agreed that permission for extensive copying of this thesis for scholarly purposes may be granted by the professor(s) who supervised the thesis work recorded herein or, in their absence, by the Head of the Department of Chemical and Biological Engineering or the Dean of the College of Graduate Studies. Copying or publication or any other use of the thesis or parts thereof for financial gain without written approval by the University of Saskatchewan is prohibited. It is also understood that due recognition will be given to the author of this thesis and to the University of Saskatchewan in any use of the material of the thesis.

Request for permission to copy or to make other use of material in this thesis in whole or in part should be addressed to:

Head of the Department of Chemical and Biological Engineering

University of Saskatchewan

57 Campus Drive

Saskatoon, Saskatchewan

S7N 5A9

Canada

Abstract

Fluidized bed reactors are utilized in a variety of applications from hydrocarbon cracking to drying of mineral ore to coating of pharmaceutical pills. A proper understanding of bed hydrodynamics is essential to properly design, operate and control the process. Intrusive and non-intrusive measurement techniques have been utilized to study various aspects of fluidized bed behaviour. Electrical Capacitance Tomography (ECT) has been utilized to determine the distribution of gas-solid mixture in the bed. The Digital Image Analysis Technique (DIAT) is used to determine the bubble behavior in two-dimensional beds. The bubble behavior has not been studied by ECT. The premise of this research is to test a new technique by combining ECT solid fraction maps with image processing techniques to determine the bubble characteristics in the bed.

Electrical Capacitance Tomography (ECT) was used to map the relative fractions of sand-air mixture in a 14 cm ID acrylic vessel at two different static bed heights. The voids were defined as the areas of gas-solid mixture with value of less than 0.25. Afterwards simple image analysis techniques were applied to isolate bubbles from the rest of the bed. The resulting data were converted into binary images to extract hydrodynamic information. The two main parameters of interest were the bubble diameter and its rise velocity. The experimental average velocities and average diameters matched the results obtained from respective correlations in the literature. However, large spreads existed for both these parameters due to the simultaneous presence of bubbles and slugs.

The experimental fluidized bed did not transition fully into the turbulent regime but has the character of a hybrid bubbling-slugging regime. This is illustrated by experimental diameters which indicate presence of bubbles and slugs simultaneously. The same information was illustrated by experimental velocity-diameter envelopes (minimum and maximum values) which overlapped for higher flow conditions. The radial solid fraction distribution illustrated the same point with an inverted “M” profile which has been associated previously with regime transition. The path of bubble rise was identified, mainly rising through the midway point between the bed’s center and its inner edge. Five different types of bubbles were

identified using the two dimensional binary images of voids. However, this technique can only be used for regimes where voids/bubbles are the main source of gas transfer to the surface of the bed.

Acknowledgements

Foremost, I would like to express my sincere gratitude to my supervisor Dr. Scott Noble who accepted me as his graduate student at a difficult time. His encouragement, guidance, and support enabled me to finish this project. I would also like to thank Dr. Todd Pugsley who initiated this project and funded this project through the initial stages.

I would like to acknowledge fellow graduate students and researchers Kurt Woytiuk, Bill Campbell, and Regan Gerspacher for making my graduate studies an unforgettable experience. I would like to thank Jennifer McMillan, Michael Wormsbacker and my former mentors at Syncrude Research Centre who inspired me to pursue graduate studies. I would like to acknowledge the financial assistance from the Department of Chemical and Biological Engineering and the Natural Science and Engineering Research Council of Canada (NSERC).

Dedication

I dedicate this thesis to the family, especially to my wonderful parents Mr. Liaquat Ali and Mrs. Parveen Akther who have always supported and encouraged me throughout my life. I would also like to acknowledge my siblings Mr. Mohammad Ali and Ms. Hijab Ali for their love and kindness. This thesis is also dedicated to the Vacarro family, especially to Kyla Michelle Vaccaro and Emma Rose Vaccaro (1987-2015).

Table of Contents

List of Tables

List of Figures

List of Symbols

A_p	Area per pixel (cm^2/pixel)
A_v	Area of Void (cm^2)
C	Capacitance measurement matrix
d_b	Bubble diameter (m)
d_{bm}	Maximum Bubble diameter (cm)
d_o	Initial bubble diameter (cm)
d_t	Bed diameter (cm)
d_v	Void diameter (cm)
E	Number of electrodes
g	Gravitational constant (m/s^2)
h	Bed height (cm)
K	Permittivity values matrix
l_{or}	Distance between orifice holes (cm)
M	Independent inter-electrode capacitance measurements
n_p	Number of pixels
R	Vessel radius
r	Bubble radius, radial distance from center of bed
S	Sensitivity matrix
S^T	Transpose of sensitivity matrix
S^{-1}	Inverse of sensitivity matrix
U_b	Rise velocity of bubbles in bed (m/s)
U_{br}	Rise velocity of single bubble (m/s)
U_c	Transition velocity from bubbling to turbulent regime (m/s)
U_k	Transition velocity from bubbling to slugging regime (m/s)
U_{gas}	Gas velocity in bed (m/s)
U_{mb}	Minimum bubbling fluidization velocity (m/s)
U_{mf}	Minimum fluidization velocity (m/s)
U_o	Superficial gas velocity (m/s)
U_{solid}	Solid velocity in bed (m/s)
φ	Bubble rise velocity parameter

1 Introduction

Fluidization is the change of powered, fine and small aggregates from a solid to a fluid like state through contact with gas or liquid. Gas-solid fluidization is characterized by two phases, a bubble phase and an emulsion phase. A non-intrusive measurement technique, Electrical Capacitance Tomography (ECT) was used to study bubble behavior through application of basic image processing techniques. This will be discussed in further detail in succeeding chapters.

1.1 Introduction to Fluidized Beds

Fluidized beds are vertical vessels containing gas-solid phases. In a gas-solid fluidized bed, solid particles sit on top of each other when no gas is flowing in the bed. As gas flow rate into the bed is increased, the solids in the bed start behaving in a fluid-like state (Park and Fan, 2006). A simple gas-solid bed consists of a vessel containing a bed of solid particles above a gas distributor. Gas distributors often support the weight of the particles and are used to inject gas into the bed in a desired manner using a pump or a gas source. A freeboard area above the particle bed exists to allow solids to disengage from the gas flow. A simple schematic of fluidized bed is showing in Figure 1.1.

The unique contacting mechanism of fluidization provides a variety of advantages from an operational point of view. Fluid-like behaviour allows for large scale continuous operations with relative ease of handling. This quality is used in a number of industrial processes such as making larger quantities of gasoline throughout the petroleum industry (Kunii and Levenspiel, 1991). They also allow for reliable operations due to isothermal conditions owing to vigorous gas-solid mixing. Fluidized beds exhibit higher rates of heat and mass transfer compared to other types of reactors. On the opposite end, there are some disadvantages associated with fluidized beds. Scaling-up the design is a difficult process due to non-linear scaling of gas-solid hydrodynamics. Solids back-mixing often lead to non-uniform residence times leading to lower conversion rates of reactants. Entrained solid particles need to be replaced on constant basis along with the possibility of reactor internals failing and erosion due to solid–reactor contact (Kunii and Levenspiel, 1991). High

operating temperatures can lead to agglomeration of solid particles leading to operational difficulties. Despite the disadvantages listed, fluidized bed reactors have been in operation for almost a century. Some of the industrial uses of fluidized beds are listed in Table 1.1

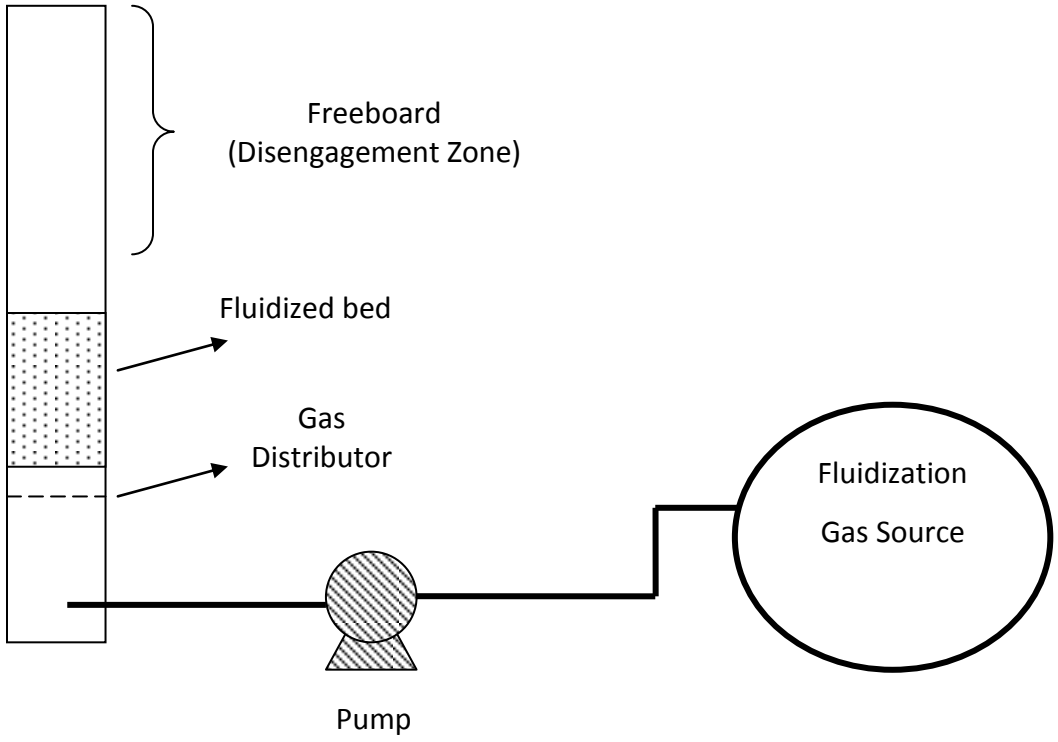

Figure 1.1. Simple fluidized bed system.

Table 1.1. Various Fluidization Processes.

Processes	Industrial Examples
Combustion	• Combustion of coal • Pyrolysis of wood waste
Chemical and Petrochemical	• Hydrocarbon cracking • Fluidized cokers
Pharmaceutical	• Granulation • Coating of pills

The fluidization behaviour of gas-solid system is strongly influenced by vessel geometry, inlet gas distributor design, distribution, type of particles and superficial gas flow rate. The bed behaviour (hydrodynamics) is described by various flowing regimes, which in turn are characterized by the gas-solid particle interaction in the bed. As fluidization gas flows through the static bed of solid particles, a point is reached when the weight of the particles is equal to the drag force from the moving gas. At this point the bed is at incipient fluidization and the gas velocity is known as the *minimum fluidization velocity* (U_{mf}). A large number of correlations have been proposed to predict the minimum fluidization velocity for a wide variety of systems (Couderc, 1985).

As the gas flow rate is increased beyond minimum fluidization conditions, instabilities are introduced into the bed resulting in formation of gas bubbles above the gas distributor at minimum bubbling velocity U_{mb}. Initially smaller bubbles are formed and they move up in the bed. As the flow rate is further increased much larger bubbles are formed as a result of bubbles coalescing into larger ones (Kunii and Levenspiel, 1991). Additional increase in the gas throughput induces slugs in the bed at slugging velocity $U_{k.}$ Slugging is said to be the mode of operations when the bubble size is equal or larger than two thirds of the bed diameter. A further increase in gas flow creates more uniformly sized bubbles and a regime transition takes the bed from bubbling/slugging to a turbulent bed at a transition velocity U_C. Further increasing the gas flow leads to solids particles being entrained in the gas stream and carried out of the bed. This ability to transport particles is utilized in circulating beds in petroleum and petrochemical industry (Kunii and Levenspiel, 1991). These regimes have distinct flow behaviour and are used in various industrial processes to take advantages of their unique qualities to maximize operational productivity. Figure 1.2 maps the progression of fluidization regimes described above.

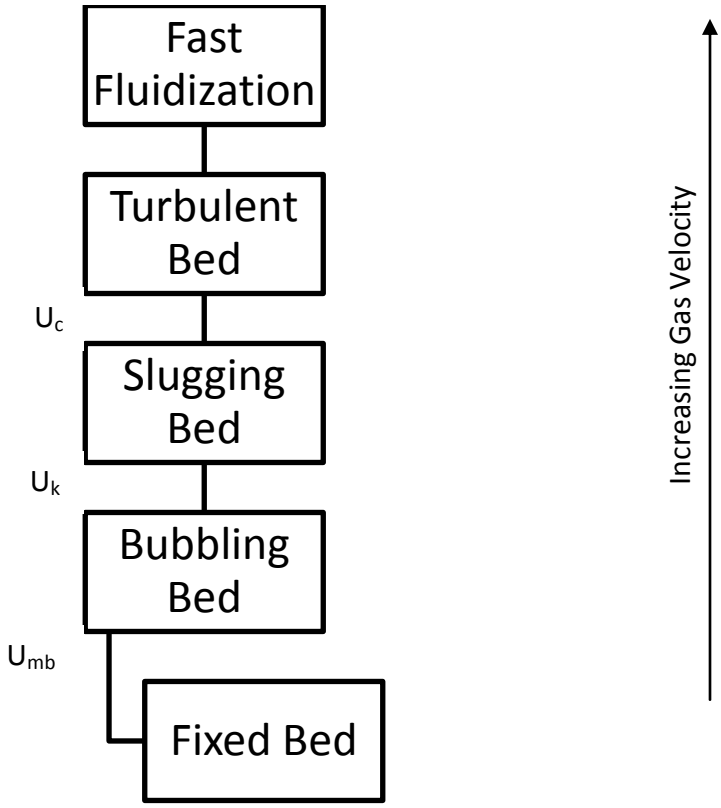

Figure 1.2. Fluidization regimes for non-circulating beds with transition velocities between regimes. Minimum Bubbling Velocity (U_{mb}), Slugging Velocity (U_k) and Turbulent Velocity (U_c).

Fluidization behaviour is largely a function of particle type. A simple but very useful system to classify particles was devised based on the density difference of particles and fluidizing gas at ambient conditions (Geldart, 1973). The four particle types have been described below and the relative boundaries of different types can be seen in Figure 1.3.

- Geldart A: These "aeratable" particles have small mean size and low density. They fluidize easily and the bed expansion occurs before bubbling velocity is reached (where $U_{mb} >> U_{mf}$). Bubble size is strongly related to particle size distribution and particle size. There is a high rate of gas exchange between bubbles and rest of the bed. Bubbles have a maximum limiting size before splitting occurs. Example includes fluid cracking catalyst (FCC).

- Geldart B: These "sand-like "particles are of medium size and density, with sand being a prominent example. Bubbling occurs at minimum fluidization velocity (i.e. $U_{mb} = U_{mf}$). Bubble size is generally independent of particle size and size distribution. Bubbles exhibit no maximum size limit and can be as large as vessel's diameter.
- Geldart C: These small sized particles are difficult to fluidize. Often known as "cohesive" particles, these are difficult to fluidize under normal circumstance. Gas flows mainly through channels. Flour and starch fall into this category.
- Geldart D: These are large, dense "spoutable" particles with fluidization taking place at higher velocities. The bubbles rise slowly and coalesce to larger bubbles. At very high gas flow rates jets are formed, coffee beans and metal ores belong to this group.

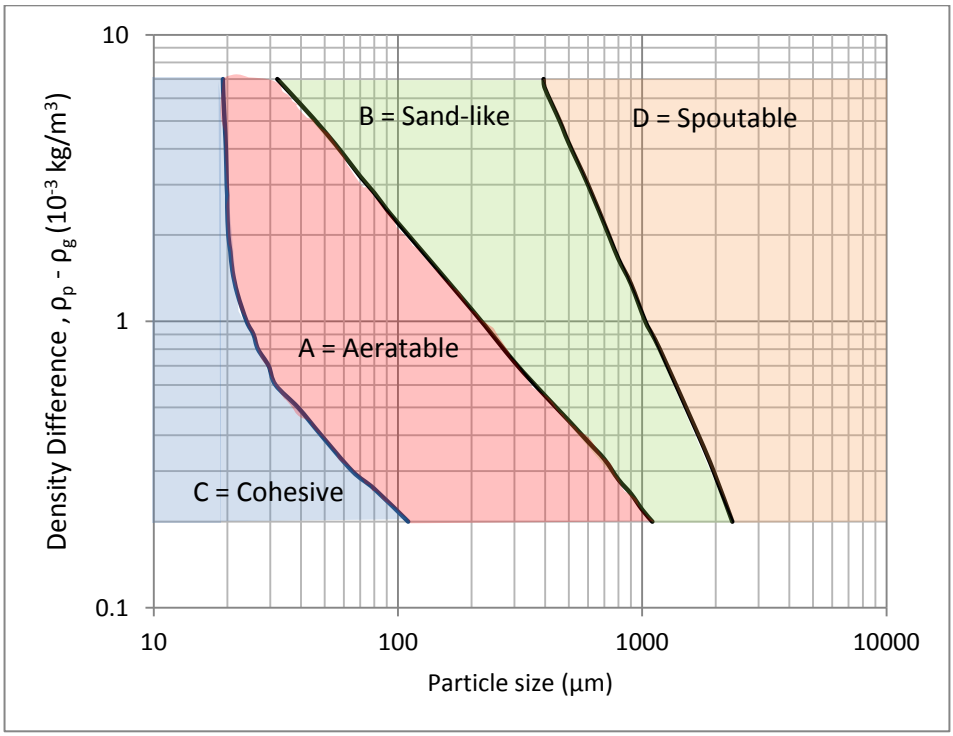

Figure 1.3. Geldart particle classification with respect to particle size and difference in particle density and fluidizing gas. Geldart A and B fluidize easily and uniformly while Geldart C and D require special conditions to fluidize.

1.2 Outline of Thesis

The next section will review aspects the bubbling fluidization regime and bubble characteristics. Various measurement techniques utilized in fluidization will be discussed. The focus will be on ECT, its working principles and how it has been used previously in fluidization research. Chapter 2 will discuss the experimental apparatus and image extraction and processing algorithms developed for bubble parameter measurements. This will be followed by discussion of results in chapter 3 with main focus on bubble rise velocity and bubble diameter. Bed behaviour will be discussed covering distribution of bubbles and solids in the bed. The last chapter will deal with conclusions and recommendations on how this technique can be used to further study bed hydrodynamics.

1.3 Bubbling Fluidized Beds

Bubbling fluidized beds derive their name from the presence of gas bubbles in the bed. Bubbles can be defined as regions in the bed with low solid concentrations, while regions of high solid concentrations are known as the emulsion phase. The bed hydrodynamics (i.e. movement, character of bubbles, interaction of solid and gas phases) in a bed play an important role in determining the quality of fluidization. Therefore significant efforts have been directed towards understanding the various aspects of bubbles and how they interact with other bed elements. Before proceeding it is important to review some aspects of bubbling fluidized beds. Other details like gas-solid mixing patterns, interaction with reactor internals etc. pertaining to this regime can be found elsewhere (Park and Fan, 2006; Kunii and Levenspiel, 1991).

Studies of three dimensional (usually cylindrical) and two-dimensional (i.e. a bed formed by two parallel plates at a close distance) bubbling fluidized beds have resulted various theoretical models quantifying bubble behaviour in the bed (Davidson and Harrison, 1963; Kunii and Levenspiel, 1991). “Two-phase” theory was one of the first models describing bubbles dividing the bed into gas and emulsion phases. The model postulates that all gas in excess of that required for minimum fluidization moves through the bed in form of bubbles, while the emulsion phase stays at minimum fluidization conditions. However, later

investigation showed that the two-phase model oversimplifies the bed behaviour in terms of gas in bubbles and flow patterns of emulsion phase (Kunii and Levenspiel, 1991).

Kunni and Levenspiel (1991) also presented a simple model pertaining to bubble behaviour. Even though this model deviates from reality in terms of bubble shape, its predictions are similar to other models in terms of solid-gas pattern around the bubbles. This model describes the motion of rising gas and solids for two- and three-dimensional beds and is based on the following postulates:

a) Bubbles are solid free circular zones of gas moving upward through the bed. They are spherical in three dimensional (3D) beds and cylindrical in two-dimensional (2D) beds.
b) Solid particles move as an inviscid fluid as they encounter rising gas bubbles.
c) Gases flows in the emulsion phase flows as incompressible fluids satisfying Darcy's law.

$$\left(U_{Gas} - U_{Solid}\right)_x = -k\frac{dp}{dx} \tag{1.1}$$

where; U_{gas}, U_{solid} are the gas and particle velocities, dp/dx is the pressure gradient in the vertical direction and k is a constant depending on the properties of the flowing fluid. These postulates quantify the movement of solids and gases, and the pressure gradient around the bubble resulting in a non-spherical bubble shown in Figure 1.4, adapted from (Kunii and Levenspiel, 1977). Gas flow patterns around and into the bubbles are function of relative bubble rise velocity. This quantifies the emulsion-bubble boundary which is important for determining various hydrodynamic parameters.

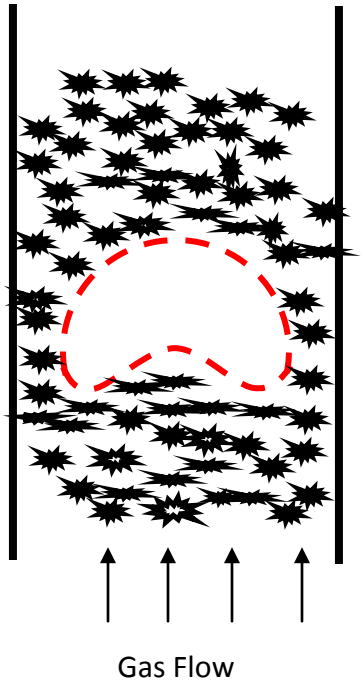

Figure 1.4. A side cross section of an idealized bubble in a fluidized bed.

A bubbling bed without reactor internals (i.e. baffles, tubes etc.) behaves in a less complicated manner when compared to a bed with internals. As bubbles move up in the bed they cause increased gas-solid mixing leading to homogenous thermal conditions in fluidized bed. Initial investigations showed that gas is exchanged between bubble and emulsion phases, leading to enhanced mass transfer (Kunii and Levenspiel, 1991). Bubbles eventually rise up and erupt at the bed surface leading to intense solid movement in the bed. Large bubbles moving up the bed take much of the gas with them, thus limiting mass/heat transfer. For Geldart B particles bubbles can grow to the size of bed diameter. Solid back mixing and the presence of large bubbles can severely limit the effectiveness of the reactor, and steps are taken during the reactor design stages to overcome these limitations.

Various bubble properties such as size, shape, rise velocity, flow of gas/solids into and out of the bubble and frequency play an important role in determining the quality of the process being carried out. Furthermore, the presence of various internals (i.e. baffles, heat exchanger pipes etc.) in fluidized beds introduces complexity to the process (Bi et al., 2005).

These factors complicate the process of studying bubbles in three dimensional laboratory, pilot scale and industrial beds. Nevertheless, because of the importance of bubbles, a significant amount of research has been focused on determining and describing the hydrodynamics of bubbling and turbulent regimes (van Lare et al., 1997; Clift and Grace, 1985; Lim et al., 1995; Bi et al., 2005).

1.3.1 Bubbles in Fluidized Beds

Bubbles in beds of Geldart A and B particles are formed when gas entering the bed encounters solid particles at and beyond the minimum fluidization conditions. Studies aimed at studying bubbles in fluidized beds have been directed towards describing the mechanism of bubble formation, their mechanism of rise, rise velocity, size and their interaction with rest of the bed elements. There is a significant amount of interaction among the bubbles and this further complicates the interaction between emulsion and bubble phase. Bubble interaction studies are concerned with modeling motion of bubbles, bubble coalescence and their interaction with rest of the bed (Clift and Grace, 1985).

In order to predict bed behaviour, a number of studies have been undertaken to characterise bubble rise velocity and diameter. This has led to a number of empirical correlations predicting the two parameters. The literature suggests that there are no “universal” equations or correlations for predicting these parameters (Karimipour and Pugsley, 2011; Kunni and Levenspiel, 1991). These empirical and semi-empirical correlations are functions of particle type, bed diameter and type of gas distributor. There are more than 15 correlations predicting bubble diameter and about 6 correlations predicting bubble rise velocity. These correlations were developed for specific particle types, bed diameters, gas distributor and gas flow rates. Another limitation in comparing the results from these correlations was the use of a wide variety of measuring techniques. Also, many of these correlations were developed using 2D beds because of the complex behaviour of bubbles in 3D beds. Therefore, one has to be careful when using one or more correlations as a standard measure. Another concern in narrow beds is the transition from bubbling to

slugging regime. Kunni and Levenspiel (1991) have provided some guidelines regarding slugging regime.

Karimipour and Pugsley (2011) compared a wide number of correlations using the square difference between the correlation values and experimental data pertaining to bubble size and their rise velocity. Some of the correlations corresponding to the system in FLASK (Fluidization Laboratory of Saskatchewan) are listed in Table 1.2 (Karimipour and Pugsley, 2011; Kunni and Levenspiel, 1991).

Table 1.2. Bubble Size and Rise Velocity Correlations.

Correlation	Equation	Applicable System
Diameter		Particle Type
Choi et al.	$(U_o - U_{mf})(d_v - d_o) + 0.474g0.5\ (d_v^{1.5} - d_o^{1.5}) = 1.132(U_o - U_{mf})h$	Geldart B
Mori and Wen	$\frac{d_{bm} - d_b}{d_{bm} - d_o} = \exp\left(-\frac{0.3h}{d_t}\right) d_{bm} = 1.87 d_o$	Geldart B
Werther	$d_b = d_o[1 + 0.272(U_o - U_{mf})]^{1/3} (1+0.0684h)^{1.21}$	Geldart A, B & D
Velocity		
David and Harrison	$U_b = U_{br} + (U_o - U_{mf})$ $U_{br} = 0.71\ (gd_b)^{1/2}$	Geldart B
Werther	$U_b = \phi(gd_b)^{0.5}$ ϕ is parameter based on bed diameter	Geldart A & B
Steward and Davidson	$U_b = U_o - U_{mf} + 0.35(gd_t)^{1/2}$	Geldart B & D

1.4 Measurement Techniques for Fluidization

A significant amount of research has been directed towards understanding bubbling bed hydrodynamics because of their effects on various fluidized-bed reactor parameters such as residence time, gas-solid mixing, product yield and quality. Both intrusive and non-intrusive techniques have been widely used to study various aspects of bed hydrodynamics. The measurement techniques can be divided broadly into industrial measurements and research measurements.

Industrial measurements are used to observe process parameters rather than studying the fundamental fluidized bed behaviour. Pressure measurement, a non-invasive and relatively easy to implement measurement technique is commonly used to assess the reactor performance. Pressure probes have been used to observe macro bed behaviour. Examples include bed hydrodynamics, solids distribution, bubble frequency and agglomeration of solids (Bi et al., 2005; Lim et al., 1995). Another common process measurement used to measure reactor performance is temperature. Heat transfer probes have been installed in industrial beds to determine local solid fraction, regime transitions points and to indirectly measure local solids flow rates (Werther, 1999). Suction probes have been used to determine the local solid flux in various reactor components (i.e. cyclones, risers etc.). Gamma-ray tomography has been used by various industrial operators to determine solid distribution in various small and large sized reactors (Martin et al., 1992). Industrial research results are generally kept confidential due to their proprietary nature. Table 1.3 at the end of this section lists some of the measurement techniques used in fluidization along with their applications.

Table 1.3. Measurement techniques utilized in fluidization research.

Parameter Measured	Measurement Technique
Solids movement and concentration (Werther, 1999)	• Fibre Optical Probes • Laser Doppler Anemometry (LDA) • Phase Doppler Anemometers (PDA) • Acoustic Emission
Fluidization Regime Transition (Bi et al., 2005; Lim et al., 1995)	• Bi-optical Probes • Pressure Probes • Capacitance Probes
Bubble Physical Properties (Shen et al., 2004; Werther, 1999)	• Reflective Probes • X-ray photography • Hot wire anemometer • Digital Imaging • Tracer Tracking
Gas-solid Behaviour (Chaplin and Pugsley, 2004)	• Radioactive Particle Tracing • Gas Tracing • X-ray/ γ-ray Tomography • Capacitance/Resistive Tomography • Positron Emission Tomography

In contrast, a large amount of academic research using invasive and non-invasive techniques pertaining to various aspects of fluidization can be found in literature (Ellis et al., 2004; Lim et al., 1995; Werther, 1999). Non-invasive measurement techniques have the benefit of not inducing any disturbance into the system, thus measuring the phenomena as it exists. Some of them (i.e. tomography and image-based techniques) are used in laboratory and pilot scale systems. However, their applicability to large industrial systems is limited due to large scale operations. One of the first and most commonly used non-intrusive techniques is measurement of pressure at various points in the fluidized bed. This technique has been utilized to assess the bed hydrodynamics in a wide variety of systems (Ellis et al., 2002; Chaplin and Pugsley, 2004; Wormsbecker et al., 2009; Chirone at al., 2006).

Another category of non-intrusive techniques used for flow visualization is based on image analysis or process tomographic measurements such as DIAT, ECT, EIT etc. (Caicedo et al., 2003; Makkawi and Wright, 2004). The fundamental principle behind these techniques is to divide the bed into bubble/emulsion phases, and then derive conclusions about the bed behavior.

Image analysis is the older of two, and is based on taking pictures of the system and then determining various bubble parameters from these pictures. The digital image analysis technique (DIAT) is based on taking images of a process and then applying image processing techniques to obtain relevant information of interest. Typical post processing steps include:

1. Image cropping, to exclude other environments except fluidized beds.
2. Image conversion to gray scale and then finally to binary images to delineates the bubble from the emulsion phase.
3. Noise removal, including false bubbles.
4. Parameter calculation on each of the binary voids.

DIAT and other optical measurement techniques are often limited to two-dimensional beds in a vertical plane (parallel to flow) as they are only capable of capturing the activity close to walls (Busciglio et al., 2009; Shen et al., 2004). Bubbles were categorized using digital image analysis by Lim et al. in two dimensional beds (Lim et al., 1995). Further experiments were conducted to determine bubble rise velocity, diameter, influence of humidity and bed expansion (Agarwal et al., 1997; Busciglio et al., 2009; Caicedo et al., 2003). Bubbles were characterized bubbles in beds with, and without internal tubes, and developed correlations for velocity and bubble size. These were then extrapolated to three dimensional beds (Hull et al., 1999). This and other studies have concluded that the size of tube and tube banks orientation strongly affect the bubble behaviour in bed (Asegehegn et al., 2011). Other studies such as Rowe and Everett utilized x-ray photographic technique to develop correlations for bubble rise velocity and bubble diameter (Rowe and Everett, 1972).

Tomographic techniques differ from image analyses techniques because they are based on mathematical reconstruction of bed's state rather than taking visual pictures of the process.

The various tomographic techniques are utilized to determine the relative fractions of bubbles and emulsion phases in the fluidized bed at certain radial and axial positions. These measurement techniques include radiation based x- or γ- ray transmission tomography, x-ray/neutron transmission radiography, positron emission, x-ray diffraction tomography and electrical capacitance tomography (ECT). A thorough review of various tomographic measurements applied to fluidization can be found in literature (Chaouki et al., 1997; Werther, 1999). These and other tomographic techniques have been used to study a wide variety of chemical reactors and flow applications i.e. pipe flow, packed beds, fluidized beds etc. (Makkawi and Wright, 2004; Ramaswamy et al., 1997; Toye et al., 1997).

1.5 Electrical Capacitance Tomography

This thesis focuses on utilizing Electrical Capacitance Tomography (ECT) to study bed hydrodynamics. Therefore it is pertinent to review how ECT measurements are made.

1.5.1 Introduction to ECT

ECT is utilized to obtain the spatial distribution of dielectric materials by measuring the capacitance the between different sets of sensing electrodes. These capacitance values are used to obtain the permittivity distribution in a bed, with permittivity defined as the dielectric material's ability to affect the electrical field. The solid-gas distribution is then determined from the permittivity values based on calibration. ECT offers an attractive choice for monitoring fluidized bed hydrodynamics because it enables non-intrusive in-line process monitoring. A typical ECT system shown in Figure 1.5 consists of two planes in series each consisting of 8 or 12 sensing electrodes, where the second plane sits on top of the first one. These sensing electrodes are sandwiched between guard electrodes, whose presence is vital to ECT resolution by suppressing out-of-plane electrical fields.

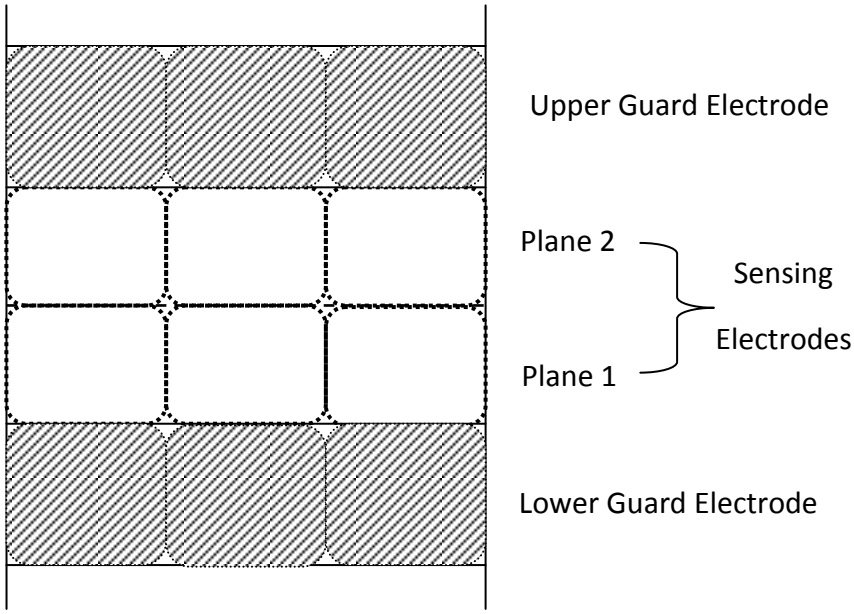

Figure 1.5. A schematic of ECT system showing guard and sensing electrode setup.

For each plane, the capacitance is measured by applying a voltage to one electrode and keeping the remaining electrodes grounded (e.g. 1-2, 1-3, 1-4 etc.), then the next set of capacitances are measured (e.g. 2-3, 2-4, 2-5 etc.). In this manner all independent capacitance measurements are made, the number of independent capacitance measurements, M, can be calculated by the following equation:

$$M = \frac{E(E-1)}{2} \tag{1.2}$$

where E is the number of sensing electrodes in the system. For an ECT system with 8 sensing there are 28 independent capacitance measurements. More detailed information regarding the design and construction of ECT sensors used in this work is available in from the system manufacturer (PTL, 1998).

Generally we are interested in normalized permittivity values. The system is calibrated by measuring the capacitance at lower permittivity (k_L) and higher permittivity (k_H) of the two dielectric materials, typically a gas and packed bed of solids. The normalized permittivity values (k_N) are calculated via at experimental permittivity (K_M) as,

$$k_N = \frac{k_M - k_L}{k_H - k_L} \tag{1.3}$$

In the case of ECT used in this project, the permittivity distribution of material in the bed is displayed on a 32 x 32 pixel grid. A circular bed utilizes about 812 of the available 1024 pixels; therefore some of the pixels lie outside the bed circumference. The tomograms obtained from ECT measurements constitute of pixels lying inside the circular bed perimeter superimposed on the square grid as shown in Figure 1.6.

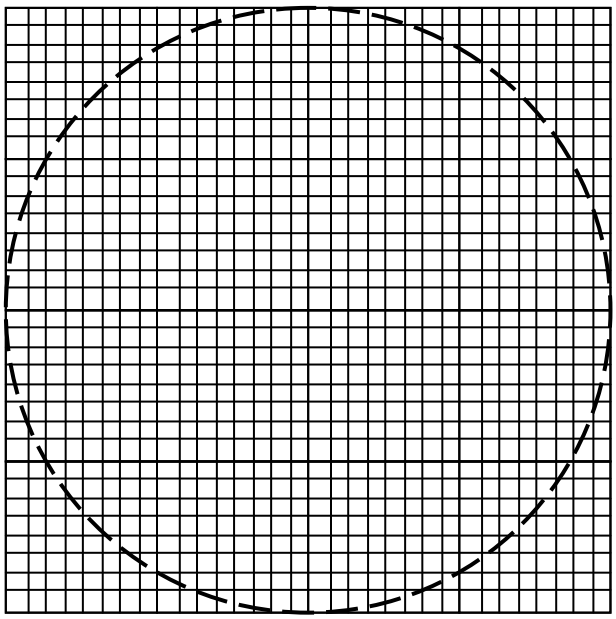

Figure 1.6. A 32 x 32 ECT pixel grid. The circle enclose 812 pixels that are used in circular ECT systems.

There are number of difficulties in obtaining the permittivity mapping from the capacitance measurements. First, a non-linear relationship exists between capacitance and permittivity. Second, for a system with 8 measurement electrodes, the number of known capacitance values (28) is far less than number of unknown permittivity values (i.e. 1024 for a 32 x 32 grid). In mathematics ECT is an example of what is known as “Inverse Problem”. In order to solve this problem (i.e. obtaining permittivity values from capacitance) a number of reconstruction algorithms have been developed to study fluidized beds, oil pipelines and

pneumatic conveying. Some of these algorithms have been revised and categorized for their accuracy in reconstructing the images of objects in bed (Yang et al., 2003). For this project the permittivity distributions inside the bed was determined by using the Linear Back Projection (LBP) algorithm. The readers are referred to literature for a detailed mathematical description of how LBP is used to reconstruct the bed's permittivity concentration (PTL, 1998).

The LBP is a simple method used to reconstruct the permittivity distribution from measured capacitance and sensitivity maps. ECT in this project is used to measure the cross-sectional permittivity distribution in the bed at a specific measurement plane, the guard electrodes at either ends suppress the electrical fields to increase ECTs axial resolution. To overcome the limitations of ECT Electrical Volume Capacitance Tomography (ECVT) is being developed to study multiphase fluid systems. ECVT's main advantage over conventional ECT is that fast moving objects in the system can be quantified volumetrically and three dimensional structures as they appear in the bed can be generated unlike ECT, which only provides quasi-3D images obtained from stacking of two dimensional permittivity distributions. Readers are referred to papers and dissertations for detailed working and image reconstructions of EVCT (Marashdeh, 2006; Du et al., 2007).

1.5.2 Application of ECT to Fluidized Systems

Electrical capacitance tomography has been applied to measure various quantities in fluidization. Table 1.4 presents some of the studies done using ECT as the instrument of choice. It should be noted that this is not an exhaustive list but rather presents various fluidization aspects investigated via ECT (Du and Warsito, 2003; Makkawi, 2002; Mckeen and Pugsley, 2002; Du et al., 2005; Warsito and Fan, 2001; Weins and Pugsley, 2006; Marashdeh, 2006).

A thorough review of ECT literature pertaining to fluidization suggests that various fluidization aspects such as solid fraction profile, characterization and transition points of various fluidization regimes, and local and global bed behaviour have been investigated (Chaouki et al., 1997; Warsito and Fan, 2001; Makkawi and Wright, 2002; Malcus et al.,

2000). Other complex behaviours such as wet granule hydrodynamics, effects of fines addition and pressurized fluidized bed behaviour have also been studied using ECT (Deen et al., 2010; Rimpiläinen, 2012).

Table 1.4. Fluidization Research by means of Electrical Capacitance Tomography

Source	Bed Diameter (m)	Application	Reconstruction Algorithm
Du et al.	0.1, 0.2	bubbling/turbulent fluidized bed	Neural Network multicriteria optimization image reconstruction (NNMOIRT)
Du el al.	0.05, 0.1, 0.3	Bubbling beds	NNMOIRT
Makkawi & Wright	0.15	bubbling/turbulent beds	Linear Back Projection (LBP)
Rimpiläinen et al.	Conical bed	Bubbling bed	
McKeen & Pugsley	0.14	Bubbling bed	LBP and Iterative LBP
Makkawi & Wright	0.15	Bubbling bed	Iterative LBP
Pugsley et al.	0.14, 0.19	Circulating bed/Bubbling	LBP and Iterative LBP
Warsito & Fan	0.1	Bubbling bed	NN-MOIRT
Weins & Pugsley	Conical bed	Bubbling bed	Iterative LBP
Du et al.	0.1	Circulating/Bubbling bed	3D-NN-MOIRT

In fluidization, transition points (i.e. moving from one regime to another) are of interest because of their distinct hydrodynamic behaviour. Early investigations relied on pressure probes to measure various regimes. Electrical capacitance tomography was utilized to determine four distinct fluidization regimes (Makkawi, 2002). The authors measured solid fraction distribution in the bed and applied various analyses (i.e. average solid fraction analysis, standard deviation of solid fraction, frequency and amplitude) on solid fraction signals. The results from these analyses allowed the authors to identify four distinct fluidization regimes (i.e., single bubble, slugging, turbulent and fast fluidization).

Du et al. applied ECT measurements to small, medium and larger beds (Du et al., 2005). The authors observed slugging in smaller 0.05 m I.D. bed, while in larger 0.1 m and 0.30 m beds bubble swarms moving upwards were observed. The larger beds exhibited an early

transition to turbulent regimes compared to smaller beds. It was also concluded that bubbles affect bed hydrodynamics more prominently in smaller beds as shown by larger standard deviation of solid fraction in smaller beds. In another study, the same authors studied bubbling and turbulent regimes (Du and Warsito, 2003). The authors calculated the boundary between the bubble and emulsion phase to be a solid fraction of 0.25. The solids fraction across the bed's cross-section showed radial symmetry in the turbulent regime which was not the case in the bubbling regime. Transition velocities were also calculated, and were in agreement with those obtained from other measurement techniques providing further evidence to acknowledge ECT as a reliable tool.

Numerous studies have been undertaken to compare ECT results with established measurement techniques like pressure measurements and optical fibre probes (Du et al., 2005; Marashdeh, 2006; Pugsley et al., 2003). A 0.14 m I.D. bed with ECT sensor attached to the outer periphery was used as a part of circulating fluidized bed (Pugsley et al., 2003). ECT results were compared to intrusive fibre optic probes; it was observed that the two techniques yielded similar results except at lower velocities. The study also answered the question regarding the need to have iterations to reconstruct the ECT measurements. The authors concluded that iterations are necessary for dense fluidization. They suggested that a minimum of 100 iterations will yield reasonable results using LBP image reconstruction algorithm. However, the standard error of instantaneous void fraction profiles measured with ECT and optical fibre probe did not match. This discrepancy was attributed to the large measurement volume used. In another study solid fraction distribution within the bed was measured with ECT and optical fibre. The authors concluded that ECT and optical fibre probe yield different solid fraction distribution in bed's central portion while they yielded similar results in the wall regions. This difference was attributed to higher reflection effects in the core regions (Du and Warsito, 2003).

Wiens and Pugsley (2006) used a 12 electrode sensor conical ECT bed to study the hydrodynamics of dry pharmaceutical granules. They discovered four distinct bubble types. An "M" shaped solid fraction profile was observed, this profile was attributed to

transitioning from bubbling to turbulent fluidization regime. Another study using the same conical bed looked at the drying hydrodynamics of wet granules and as a result the author suggested designing a new sensor containing an increased number of measurement electrodes to better capture the bed behaviour during the drying process (Rimpiläinen et al., 2012).

1.6 Knowledge Gap and Objectives

This research is aimed at studying the bubble behavior in a fluidized bed using Electrical Capacitance Tomography (ECT). Fluidized beds have been studied in a wide variety of ways due to their importance in industrial processes (Kunii and Levenspiel, 1991). Bubble parameters such as velocity and diameter play an important role in fluidization operations. Various methods have been used to determine these parameters using a wide variety of measurements (Karimipour and Pugsley, 2011). Electrical capacitance tomography (ECT) provides an average cross-sectional distribution of materials inside a vessel and is generally complimented with another measurement technique such as measurement of pressure fluctuation or optical fibre probes (Pugsley et al., 2003). The Digital Image Analysis Technique (DIAT) is based on taking images of a process and determining the respective parameters of interest. ECT has been used to determine the average/ global bed behavior instead of looking at individual bubbles and their associated parameters.

Despite identifying bubbles as an important participant in bed dynamics researchers have yet to study bubbles via ECT measurements. Two major gaps have been identified in determining bubble hydrodynamics using ECT:

1. A review of ECT literature suggests that morphological (shape-based) image processing techniques have never been applied to ECT data.
2. Given the importance of bubbles in fluidized beds, they have not been characterized solely using electrical capacitance tomography.

1.7 Objectives

The overall objective of this research project was to determine if some aspects of morphological image processing techniques can be applied to ECT generated solid fraction maps to obtain information on fluidized bubble behavior. In order to study the bubbling behaviour of Geldart B (i.e. sand) fluidized bed at low fluidization velocities the following steps were deemed necessary:

1. Develop an algorithm to apply image analysis to the solid fraction maps to yield various bubble parameters.
2. Verify ECT's ability to independently measure the velocity and diameter of objects in the bed and then use it to measure these bubble properties.
3. Using the results of bubble characteristics and bubble behavior, discuss and how they relate to bed behavior and existing correlations.
4. Identify the limits of this application and propose a future course of action.

2 Experimental Apparatus and Measurement Technique

2.1 Experimental Set-up

Electrical capacitance tomography was used to obtain the permittivity distribution of air-sand mixture by measuring the inter-electrode capacitance. The biplanar ECT sensor in the Fluidization Laboratory of Saskatchewan (FLASK) is shown in Figure 2.1. It consists of two guard electrodes and eight sensing wrapped around a 0.14 m I.D. acrylic tube. A schematic of the electrode arrangement is shown in Figure 2.2.

In-house MATLAB® (MathWorks, Natick MA) codes utilizing iterative linear back projection (LBP) were used to study bed hydrodynamics (Chaplin and Pugsley, 2004). Mckeen and Pugsley (2002) showed that using more than 200 iterations with the parallel capacitance model yields good agreement between the size of object placed in the bed and the reconstructed image.

The bed material was Geldart B sand with a Sauter mean diameter of 234 µm. Two static bed heights (i.e. height of bed without inlet air flow) of 42 cm and 49 cm measured from the gas distributor were chosen such that the bed material overlapped both sensing electrodes with bed height to bed diameter ratios of 3.0 and 3.5 respectively. Higher values were not chosen because of the lack of pressurized air supply. A stainless steel, square-pitched gas distributor with an open area of 3.4 % was installed. The inlet gas flow was limited by pumping capacity and four flow rates of 100, 200, 300 and 400 liters per minute (LPM) with an uncertainty of ±25 LPM due to pressure fluctuations in supply were chosen. Experimental conditions are listed in Table 2.1.

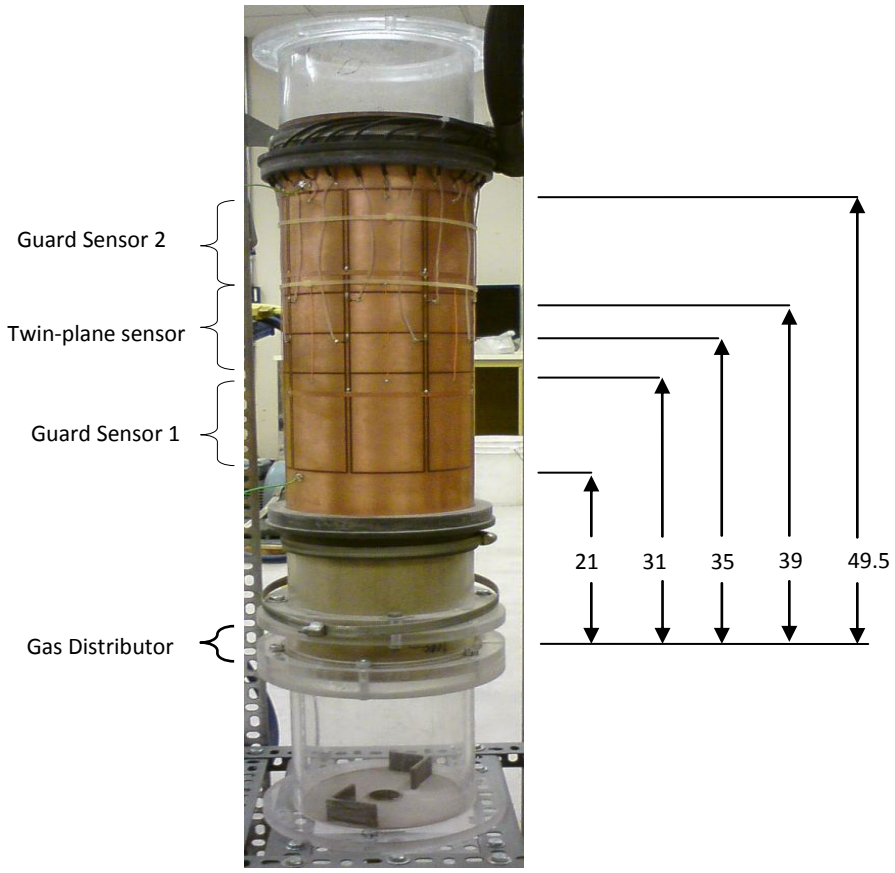

Figure 2.1. PTL's 8 electrode ECT sensor (all dimensions have units of cm).

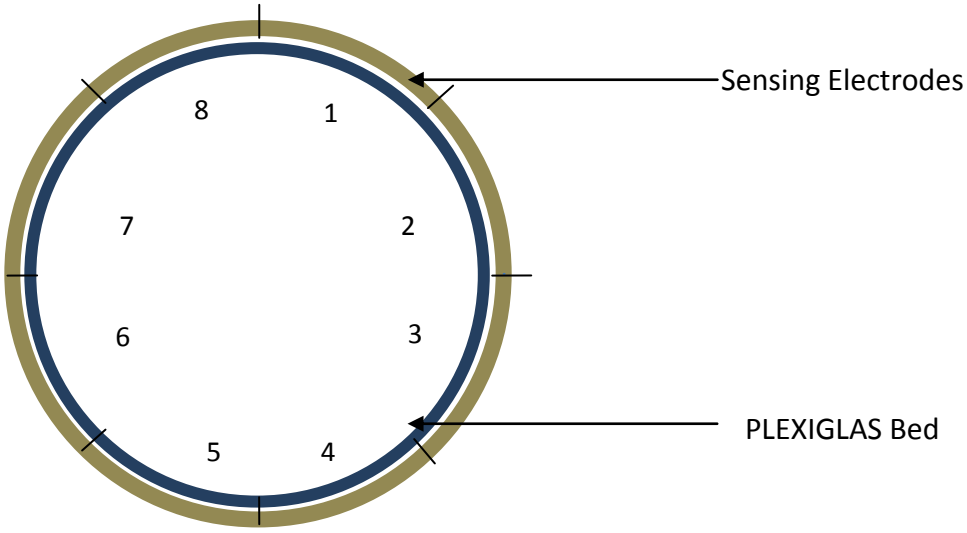

Figure 2.2. Sensing electrode arrangement outside the fluidized bed.

.

Table 2.1. Experimental Set-up Parameters.

Experimental Set-up	**Condition**
Fluidized bed column	I.D. = 0.14 m, material: PLEXIGLAS
Gas Distributor with fine mesh	Square pitched; 396 holes of 2.08 mm dia.
Bed Material	Sand, diameter = 234 µm, density = 2600 Kg/$m^{3,}$
Fluidization Gas	Air, ρ_g = 998 kg/m^3
Superficial Gas flow rate	100, 200, 300 and 400 LPM
Static Bed Height	42 and 49 cm from gas distributor
Minimum Fluidization Velocity	0.046 m/s (~43 LPM)
Sensor	Externally mounted twin plane ECT

2.2 ECT Parameter Extraction and Image Processing

Capacitance measured during operations form the basis of further analysis. The following subsections will describe how parameters were calculated from ECT measurements. The application of DIAT to ECT data will also be discussed.

2.2.1 Electrical Capacitance Tomography

To obtain the relative distribution of solids and bubbles in fluidized beds raw capacitance measurements are converted into normalized capacitance. The two capacitance values are normalized such that 0 corresponds to an empty bed and 1 corresponds to a fully packed bed of the dielectric material used for calibration, in this case sand. These normalized capacitances are valid as long as there is no change in bed material's permittivity during experimental span such as change in moisture content of the fluidizing material. Makkawi and Wright (2002) have laid down some ground rules with regards to accurately capturing the fluidized bed hydrodynamics as a function of experimental run. Following these guidelines, experimental runs were conducted after stabilizing the bed for about 60 seconds. Approximately 5000 frames of data per experimental run were collected at a frequency of 100 Hz (experimental run of approximately 50 s).

A basic iterative linear back projection algorithm (using 250 iterations) was used to reconstruct the permittivity distribution in the bed. Using in-house developed code, three different types of permittivity distributions (pixel values between 0 and 1) for each experimental run were obtained:

1. A time series of n, 32 x 32 solid fraction maps, where n is the number of frames recorded
2. A 32 x 32 solid fraction distribution averaged over time using all frames collected from a 50-second experimental run,
3. A time series of mean solid fraction for each frame versus time (set of time-mean ordered pairs),

The time-averaged 32 x 32 map has been used to construct radial profile of solid distribution in the bed. Most two-dimensional ECT research has been focused on utilizing the mean solid fraction versus time series and applying various analyses. The average solid fraction and the radial solid distribution have been used to determine regime transition points while the standard deviation of solid fraction has been utilized to determine minimum fluidization velocity (Makkawi, 2002). The time series of 32 x 32 permittivity distribution maps have been used to construct a pictorial representation of a particular frame (n) known as a tomogram. A typical tomogram is shown in Figure 2.3, where the red parts represent areas of dense solid concentration while the blue parts indicate areas of low solid concentrations.

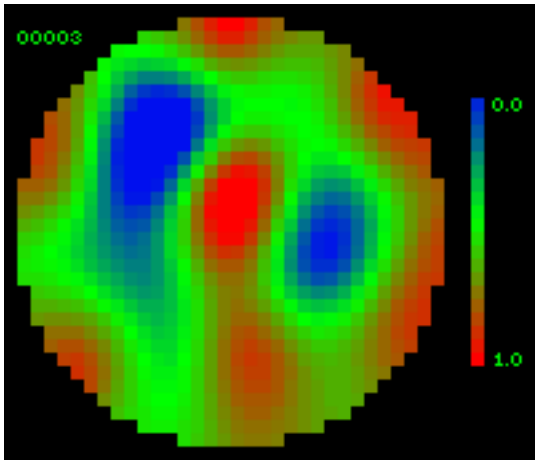

Figure 2.3. Typical tomogram from ECT. 0 represents air pockets and 1 represents solid phase.

Typical average solid fraction signals with respect to time for the upper and lower planes are shown in Figure 2.4. The reduction in solid fraction around 300 and 400 ms represents the passage of a bubble. Immediately after the bubble passes, solids move in to fill the voids leading to an increase in solid fraction around 600 and 700 ms. The bubble rise velocity is calculated by dividing the distance between the measurement planes by time difference observed in when the bubble passes the planes. Various other analyses of frequency and amplitude have been used on time series signal to determine the transition velocities.

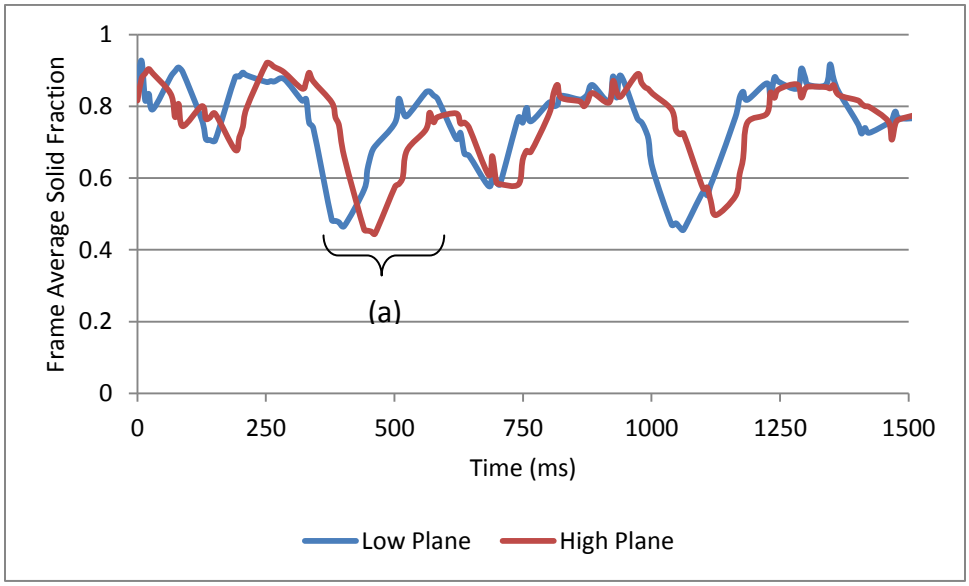

Figure 2.4. Variation in solid fraction at sensor level from passage of bubbles.

2.2.2 Application of Image Processing to ECT Measurements

In fluidization digital image process techniques are used to study two-dimensional fluidized beds (i.e. a bed formed with 2 parallel plates). It is based on converting video frames into binary images by delineating the bubble-emulsion phase boundary. Subsequently various bubble parameters are calculated by processing these images. ECT provides a map (32 x 32) of the normalized permittivity distribution in the bed illustrating regions of low and high solid concentration. An interesting question arises of whether there is a possibility of applying a component of some aspects of image analysis to ECT measurements?

As far the author is aware no studies have been done where ECT capacitance measurement have been combined with morphological image analysis techniques. The author of this research is aware of the limitations of applying image analysis techniques to ECT data because it is itself a reconstructed approximation of bed behavior. However, application of DIAT to ECT data will give an opportunity to test the applicability of combining these two techniques and whether it yields further insight into the bed behavior that cannot be obtained from conventional two-dimensional ECT analysis.

The bubble boundary needs to be defined for the application of digital image analysis (DIAT) to ECT measurements. The bubble-emulsion threshold was chosen to be a solid fraction value of 0.25 based on the work of Du et al. (2005). It is important to note that unlike sand used in this study, Du et al. used much finer fluid catalytic cracker (FCC) particles. The verification of gas-solid boundary value of 0.25 will be described in next section.

The bubble parameter extraction process was conducted using simple inbuilt MATLAB® functions. Function “im2bw” with a threshold of 0.25 was used to convert ECT permittivity maps into binary images. All values about 0.25 were converted to 1 appearing white while the rest were given a value of 0 which appeared as black. The “*imcomplement*” function was used to compute a complement image, meaning that pixel values of 1 and 0 in the binary image were swapped. In the resulting images, voids had a value of 1, and high solid fraction areas a value of 0. The resulting image was cleaned by removing all connected components (objects) containing fewer than 30 pixels using the “*bwareaopen*” function,

objects smaller than 30 pixels were judged to be random artifacts. In order to obtain parameters of interest, the objects within the binary image were connected using "*bwconncomp*" using two-dimensional connectivity of 4. This means a pair of adjoining pixels is part of the same object only if they are both on and are connected along the horizontal or vertical direction. The last step was to demarcate object boundaries, "bwboundaries" with "no-hole" and 8-connected neighborhood specification. The 'no-hole' option ignores any secondary objects inside the main object and does not demark their boundary. This was chosen because this study only concerned with the outer periphery of the bubble. In an 8-connected neighborhood all of the pixels that touch the pixel of interest are considered whether they are connected along the horizontal, vertical, or diagonal direction. In contrast in a 4-connected neighborhood, only the adjoining pixels in horizontal or vertical direction are considered part of the object.

After applying the bubble threshold the permittivity map was converted into a binary image. The MATLAB® Image Toolbox function "*regionprops*" was used to calculate various bubble parameters such as diameter, centroid (x-y coordinates) and centricity (roundness). A typical binary image showing slice of a passing bubble is shown in Figure 2.5 below with white parts indicating a void and black parts representing the rest of bed. This binary map/image formed the basis of all parameter calculations such as bubble velocity, their size and position in the bed. The results obtained from these maps were used to determine various aspects of bubble behavior such as their distribution in bed and various bubble types.

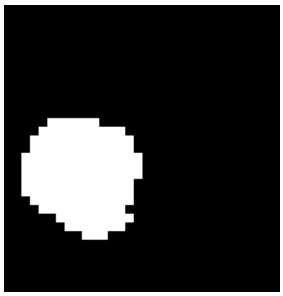

Figure 2.5. Binary image of a void (white).

The ability of image processing algorithm to capture the bubble characteristics was determined. The void-area time series should coincide with the solid fraction time series; Figure 2.6 illustrates the two signals. Solid fraction signal (dotted line) is superimposed with void area signal (solid line). A series of binary images under the graph illustrate the passage of voids as they appear to ECT. The point labelled “a” has high solid fraction i.e. there are no bubbles passing through the sensor at this point; the corresponding void area is zero. At around frame number 45 the bubble passes the upper sensing electrode as indicated by a peak, at the same time the solid fraction signal is at its minimum. These two points can be seen in the binary images image series below. While this establishes a degree of confidence in the application of digital image analysis techniques applied to ECT data, it is important to note that the two curves do not coincide exactly. This can be explained by the different nature of the two signals. The solid fraction signal is an average value of 1024 pixels. On the other hand the void area signal is based on binary images based using a bubble-solid threshold of 0.25.

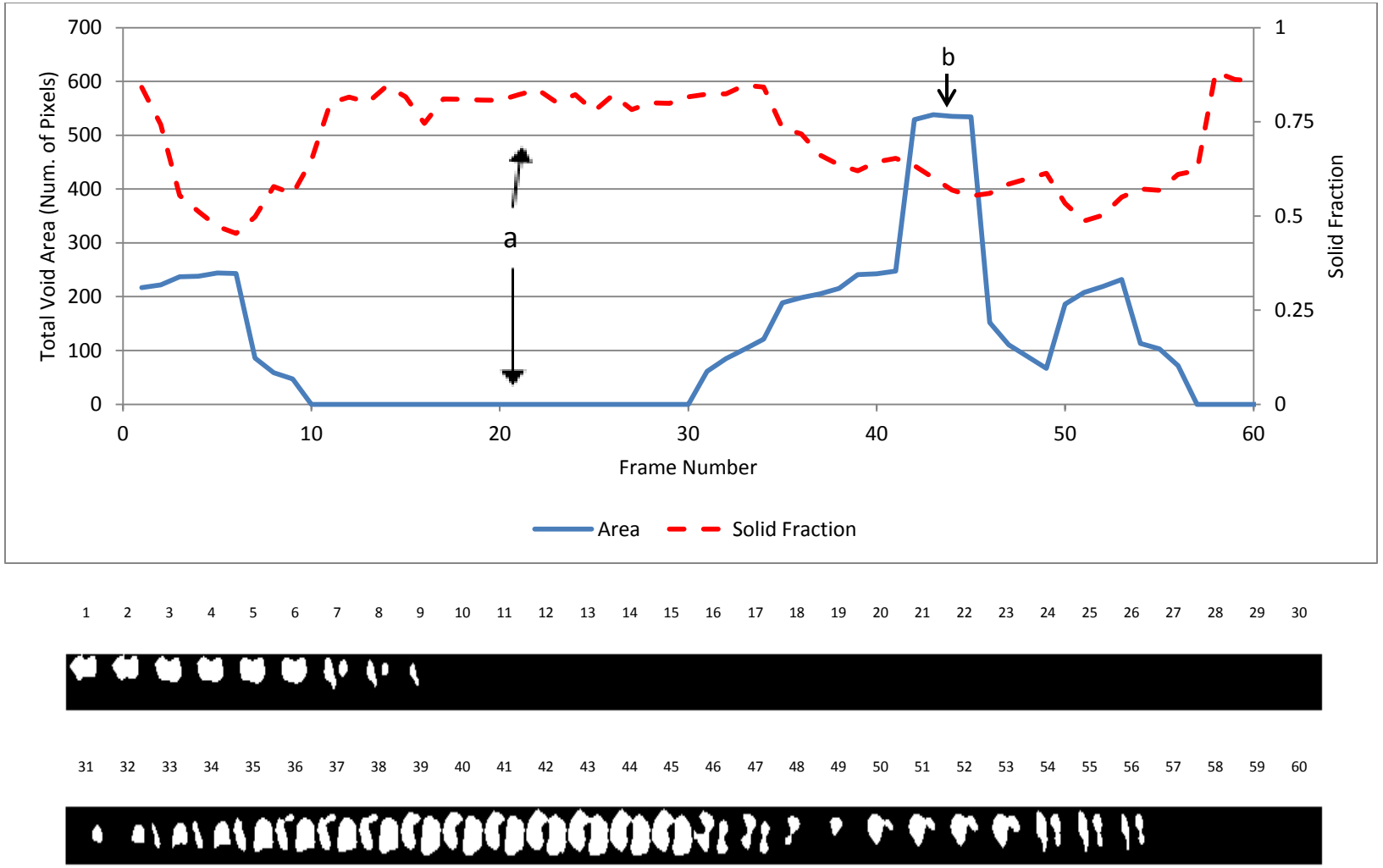

Figure 2.6. Solid fraction and void area along with binary images as a function of frame number. High solid fraction (a) corresponds to no bubbles while Low solid fraction (b) corresponds to passage of bubble at sensing level.

2.2.3 Verification of Bubble Parameters

The ability of the reconstruction algorithm to determine the bubble rise velocity and void diameter characteristics is essential to describing bed behavior. These two parameters were checked to verify ECT's ability to determine them.

An algorithm was implemented in MATLAB® to calculate the bubble rise velocities and void diameter. The void area-time series for the two sensing planes were arranged and the algorithm searched for passage of bubbles across the sensing planes. The passage of bubbles is represented by an increase and then eventual decrease in void area. The top of this peak represents the maximum area of the bubble. This maximum peak area along with the time at which it occurred was recorded for both sensing plane signals. The individual bubble rise velocity was calculated by dividing the distance between the two planes (i.e. 4 cm) by the time between the peaks (i.e. the bubble travel time). The individual bubble rise velocity and corresponding area were recorded for each bubble and an average rise velocity and bubble diameter were calculated by taking an average of all individual velocities. To check for erroneous peaks, visual observations were made to discard secondary local peaks resulting from the algorithm. An example of signal illustrating multiple peaks is shown in Figure 2.7. The figure shows void area as a function of time with peaks represent passage of bubbles through the sensing plane; the markers at the peak summit represent the void with the largest area. A local peak exists for the upper sensor at 1400 ms alongside a larger peak at 1460 ms (red arrow). The lower peak at 1400 ms was discarded as a result of manual check. Another example is the presence of two peaks around 1700 ms for the lower plane. The first of the two peaks was used to correctly determine the bubble rise velocity while discarding the other data point. The bubble diameter was obtained using the same area time series. For Geldart B particles bubbles tend to grow in size as they rise up (Kunni and Levenspiel, 1991). Therefore, the final void diameter was determined at the time of maximum void area using the upper plane's signal. The next two sections present the techniques and results used to verify the void velocity and diameter.

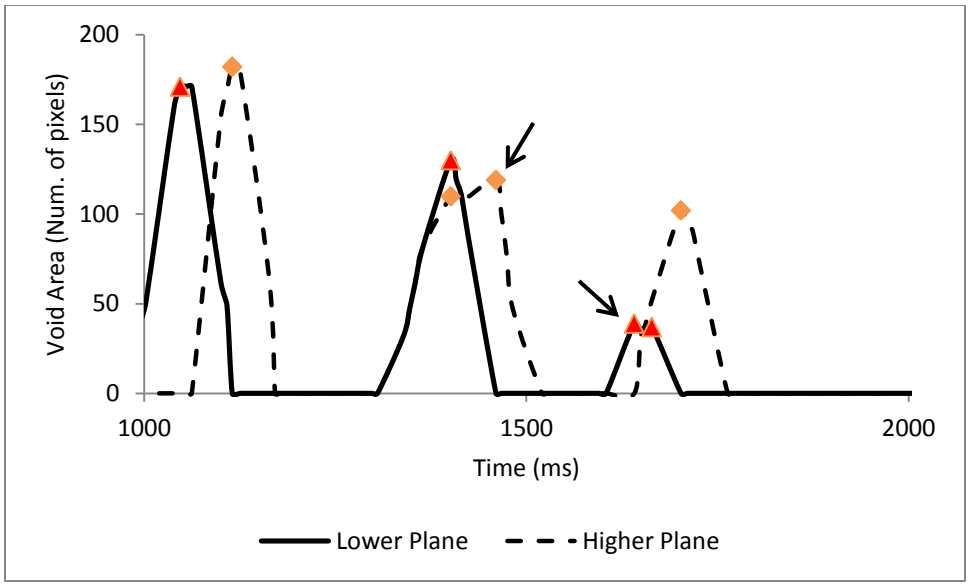

Figure 2.7. Void area signal illustrating multiple peaks for higher plane. The secondary peaks were manually removed from data.

2.2.3.1 Bubble Rise Velocity

The bubble rise velocity was checked using an external electric motor, a tennis ball attached to a fishing line and a rotary encoder. An electric motor was installed above the bed to pull the ball, simulating a bubble rising in the bed. A rotary encoder with a 1^{o} resolution and a diameter of 3.7 cm was installed externally at the bottom of bed and the fishing line was wrapped around a spool on the encoder. To facilitate the tennis ball's movement, small amounts of air were allowed to flow in the bed thus reducing friction caused by presence of sand. As the ball moved the rotary encoder spool rotated and the angular displacement with respect to time was recorded on a data acquisition system using LabVIEW©(National Instruments, Austin TX). At the same time, the ECT recorded the solid fraction disturbance in the bed due to ball's upward motion. The velocity from data encoder was calculated as follows:

- The instantaneous revolutions per second were calculated from the adjacent data points from the elapsed time and rotational count.

- This rotational speed was converted to linear speed by using the encoder diameter in form of π x d, where d was the encoder's diameter with a value of 3.7 cm.

The ECT data were processed to obtain the ball's rise velocity using the solid fraction time series. The ball rising through the bed and subsequent capacitance measurement presented two challenges. First, the solid fraction disturbance of the moving ball was not captured on the online tomograms and second the measured capacitance disturbance was very minute. This small magnitude can be due to semi-solid nature of the ball and ECT's inability to distinguish it from the sand. The change in solid fraction as the ball moved up the bed through the two measurement planes is shown in Figure 2.8. The solid fraction signal changes from 0.98 to 0.90 and then back to 0.97. This change in solid fraction was not captured in the tomograms because of the small magnitude. However, because of the clear time difference the signal was deemed to be an acceptable reference point for velocity measurement.

The resulting rising ball rise velocities from the motor and the ECT were compared are shown in Figure 2.9 along with a 1:1 correspondence line. The vertical axis represents the velocity of the rising ball obtained through reconstruction of capacitance data and the horizontal axis is the velocity of rising tennis ball from rotational encoder. With the average difference of 6.16 % between the two measured velocities and a coefficient of determination of 0.40 the two velocities do not correlate well. The difference between the velocities obtained from the two techniques can be attributed to the manner in which velocities are measured. The accumulated revolutions of the rotational encoder for the four test runs as the object moved upward are shown in Figure 2.10. The flat portions of the curves represent the start and end of test runs when the object was not being pulled. The middle portion represents the object's rise from the bottom of the bed to its surface. The non-uniformity in object's rate of rise is due to the combined effects of non-uniform motor speed and irregular superficial gas velocity for the four tests. Another very important reason why the two velocities do not match up is the slippage of wire over the encoder and the lateral movement of the ball. This can be shown by calculating the linear distance moved by

encoder throughout the experimental run. The distance calculated from the encoder data was in range of 22 cm to 28 cm which is less than the distance from gas distributor to the top of sensing plane indicating slippage if wire over the spool. It is also important to note that the velocity measured at the measuring plane representing the instantaneous velocity while the velocity obtained from the encoder is the overall rise velocity of object through the bed. In this particular situation the velocities obtained from ECD are relatively more reliable because of the various complexities involved with the encoder-motor set-up but they will have to be compared against the velocities obtained from velocity correlations.

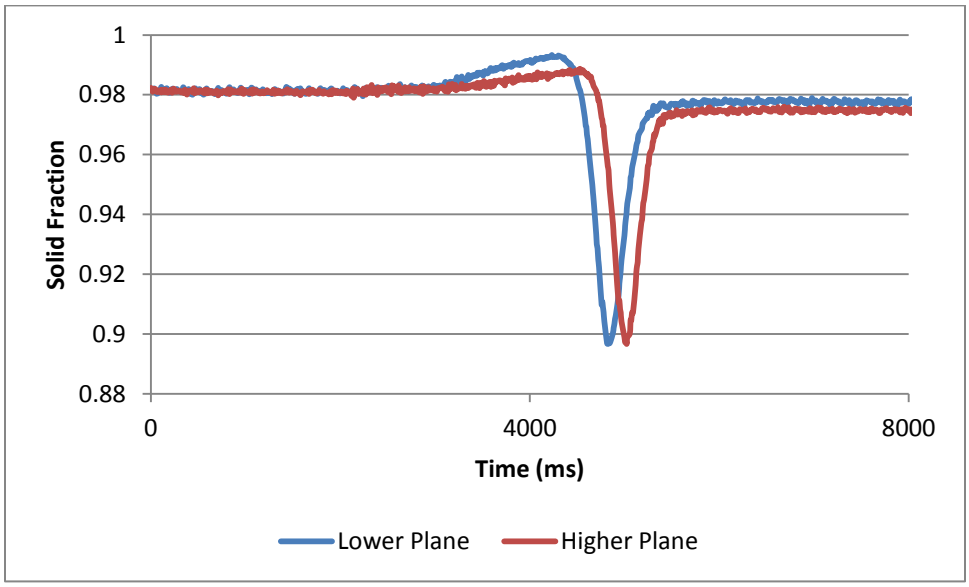

Figure 2.8. A reduction in solid fraction at sensor level as a result of rising object.

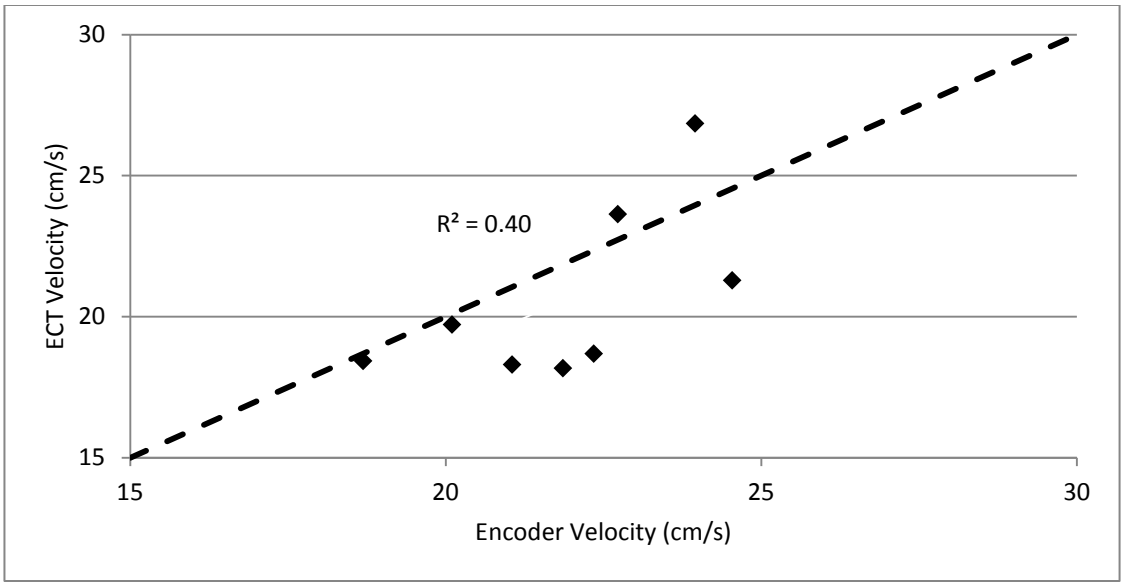

Figure 2.9. Comparison of object rise velocities from ECT and rotational encoder. The dashed line represents the 1:1 line indicating perfect correspondence between the two measurements.

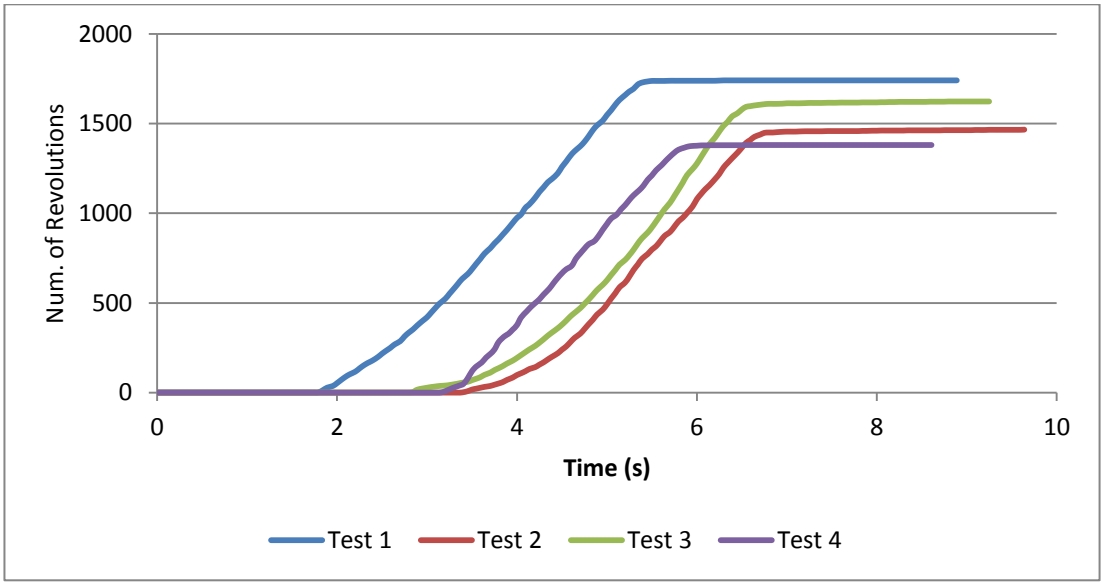

Figure 2.10. Rotational encoder revolutions with rise of object in bed. The sloped portions represents rise of the object in fluidised bed. The flat regions indicate static object.

2.2.3.2 Bubble Diameter

Bubble diameter is another important parameter of interest. A simple experiment was devised to validate iterative LBP's and image processing algorithm's ability to measure the bubble diameter. An empty acrylic tube with an outer diameter of 76 mm was inserted into a static bed filled with sand. Capacitance was measured and the data were reconstructed using LBP with 200 iterations. The build-in MATLAB® function described previously were used to determined the image area with units of number of pixels. The circular equivalent void diameter was calculated as follows:

$$d_v = \sqrt{\frac{4A_v}{\pi}} \tag{2.1}$$

Where A_v is the area of a single void; 812 is the number of pixels enclosed in the ECT vessel. There after the area of void (A_v) from binary image with units of cm^2 was calculated by,

$$A_v = A_P \times n_P . \tag{2.2}$$

Where A_p is the area of single pixel and n_p is the number of pixels obtained from MATLAB®. The area of single pixel was calculated to be:

$$A_P = \frac{0.25\pi d_t^{\,2}}{812 pixels} = \frac{\text{Area of bed}}{\text{Total Number of Pixels}} \tag{2.3}$$

A binary image of the tube obtained by using iterative LPB with the parallel model is shown in Figure 2.11 with test results shown in Table 2.2. The parallel model assumes that the permittivity of the gas-solid mixture can be obtained simply by summing the effects of the two components. These results indicate that Linear Back Projection using parallel capacitance model and the new image processing algorithm can reasonably predict the size of the objects in bed. Similar results were found by inserting an empty tube filled and a tube filled with FCC particles and then reconstructing the objects in beds (Mckeen and Pugsley, 2002). It is important to note that the acrylic tube has a solid boundary unlike bubbles whose boundary is more permeable. This can impact the bubble diameter and shape factor results.

Table 2.2. Verification of Plexiglas tube diameter.

Parameter		Parallel Capacitance Model	Series Capacitance Model
Area (Pixels)	Plane 1	238	129
	Plane 2	235	125
Exp. Diameter (in)	Plane 1	2.99	2.20
	Plane 2	2.97	2.17
% Diff	Plane 1	0.268	26.6
	Plane 2	0.898	27.7

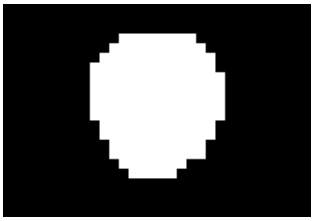

Figure 2.11. Binary image of a 76 mm (3'') acrylic tube.

The independent validation of bubble diameter and velocity results put confidence in ECT's and subsequent image processing algorithm ability to decipher some aspects of bed behaviour. These two parameters were determined for various operating conditions; the results and how they compare with other theoretical models will be presented in next section.

3 Results and Discussion

Individual bubble properties such as diameter and rise velocity were obtained from applying DIAT to the gas-solid fraction as will be presented in the next section. These measurements were compared to existing correlations pertaining to Geldart B particles. The overall bed behaviour and bubble interaction with each other is presented in section 3.2.

3.1 Bubble Properties

All the ECT measurements were taken at static bed heights of 42 cm and 49 cm. These values were chosen such that the static bed to bed diameter ratio was 3 and 3.5 respectively. This ratio ensured that the two sensing planes were below the static bed surface to capture the bed behavior. The higher bed height was limited by the capacity of the fluidization air supply apparatus. Bubble rise velocity and diameter were determined from the application of image processing techniques to ECT measurements. The bubble velocity and diameter outliers were discarded in the results presented in the succeeding sections. The outliers were defined as 1.5 times the interquartile range below the first quartile or above the third quartile. The bubble velocity and diameter results obtained experimentally are compared to correlations proposed in the literature (Karimipour and Pugsley, 2011).

3.1.1 Void Diameter

Mori and Wen (1991) empirically calculated the bubble diameter d_b at any height z in a bed by:

$$\frac{d_{bm} - d_b}{d_{bm} - d_{bo}} = e^{-0.3h/d_t}, \tag{3.1}$$

where d_{bo} is the initial bubble diameter, d_{bm} is the maximum bubble diameter and d_t is the bed diameter. They are given by the following equations:

$$d_{bo} = \frac{1.30}{g^{0.2}}\left(\frac{U_o - U_{mf}}{1/l_{or}^2}\right)^{0.4}, \text{ and} \tag{3.2}$$

$$d_{bm} = 0.65[\frac{\pi}{4} d_t^2 (U_o - U_{mf})]^{0.4}, \quad (3.3)$$

where l_{or} is the distance between the adjacent holes in gas distributor, g is acceleration due to gravity, U_o is inlet air flow in the bed and U_{mf} is the minimum fluidization velocity.

Figure 3.1 shows the distribution of void diameters obtained from processing data from ECT's upper sensing plane. The largest diameter of a series of voids constituting a bubble was chosen as the bubble diameter. The mean diameter is slightly larger for the deeper bed height of 49 cm in comparison to the shallow 42 cm bed, agreeing with previous findings (Kunni and Levenspiel, 1991). The maximum bubble diameter is identical for the two beds for every flow condition reaching the bed diameter except for the lowest flow rate of 100 LPM. At 100 LPM bubbles dominated the bed behavior for both the bed heights.

As the inlet gas flow rate is increased the maximum bubble size for both bed heights increases. Even though the measurement plane was at the same elevation for both static bed heights, bubbles in the 49 cm bed have slightly larger average diameters. The larger mean diameter for the deeper bed can be attributed to presence of slugs in the bed along with the bubbles. Disappearance of smaller bubbles along with presence of slugs reduces the range of bubble diameters in both beds. A minimum detectable bubble size exists for both conditions with deeper beds having a larger minimum bubble diameter. The exact reason as to why the beds have increasing minimum diameter was not determined but it could be due to increased interaction amongst the bubbles in deeper beds.

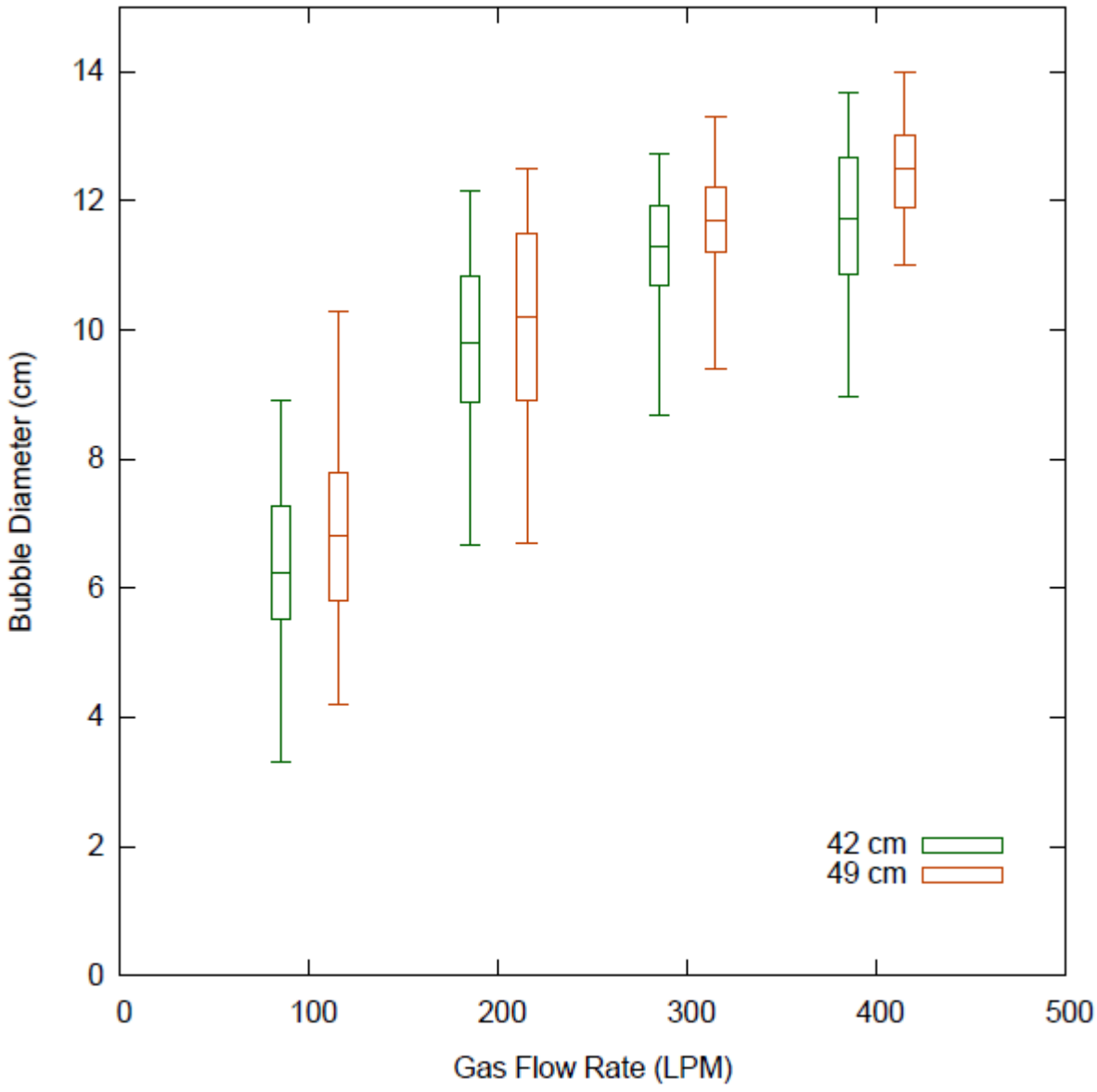

Figure 3.1. Distribution of bubble diameter in a bed of sand for two static bed heights of 42 cm and 49 cm at air inflow of 100 , 200, 300 and 400 LPM respectively. The box represent the 25th percentile, mean and 75th percentile of bubble diameter. The extreme ends of the error bar represents minimum and maximum bubble diameter.

The standard deviation of bubble diameter for both bed heights is shown in Figure 3.2. The two beds illustrate more or less the similar behavior. For the shallow 42 cm bed bubbles dominate the bed behaviour at 100 LPM but bubbles and slugs coexist in the deeper 49 cm bed. As gas flow rate is increased slugs are introduced in the shallow along with bubbles resulting in an increase in standard deviation. For the deeper 49 cm bed slugs are bubbles

are replaced with slugs thus reducing the standard deviation. However as the flow increases slugs dominate both beds narrowing the size difference among the bubbles resulting in reduction of standard deviation. The increase in standard deviation for both cases at the 400 LPM air flow indicates a more turbulent bed behavior.

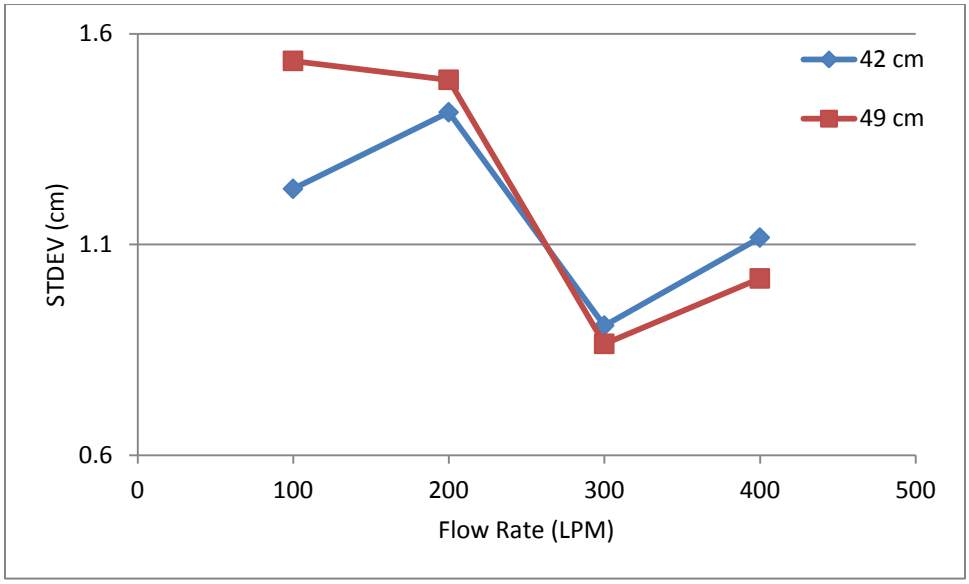

Figure 3.2. Standard deviation of bubble diameter for the two bed heights.

The upper set of sensing electrodes is located at a distance of 39.4 cm above the gas distributor. This value was used in the Mori and Wen (1991) correlation to calculate the bubble diameter instead of static bed heights. The experimental bubble diameters for the two bed heights yielded similar results. Therefore a mean bubble diameter of the two beds at every operating condition was taken and compared with diameters obtained from correlations. The experimental and theoretical void diameters from the correlation are shown in Figure 3.3. The experimental results tend to level off as the bubble diameter approaches the bed diameter but the correlations are increasing. Similar results were obtained in a deeper two-dimensional bed where bubble size reached a maximum size and then levelled off (Shen et al., 2004). The presence of slugs yields higher void diameter values for the flow rates of 200 LPM and 300 LPM. The introduction of slugs indicate onset

of slugging behaviour, but a 14 cm diameter fluidized bed would require static bed height of 95 cm for slugging to completely set in (Kunni and Levenspiel, 1991).

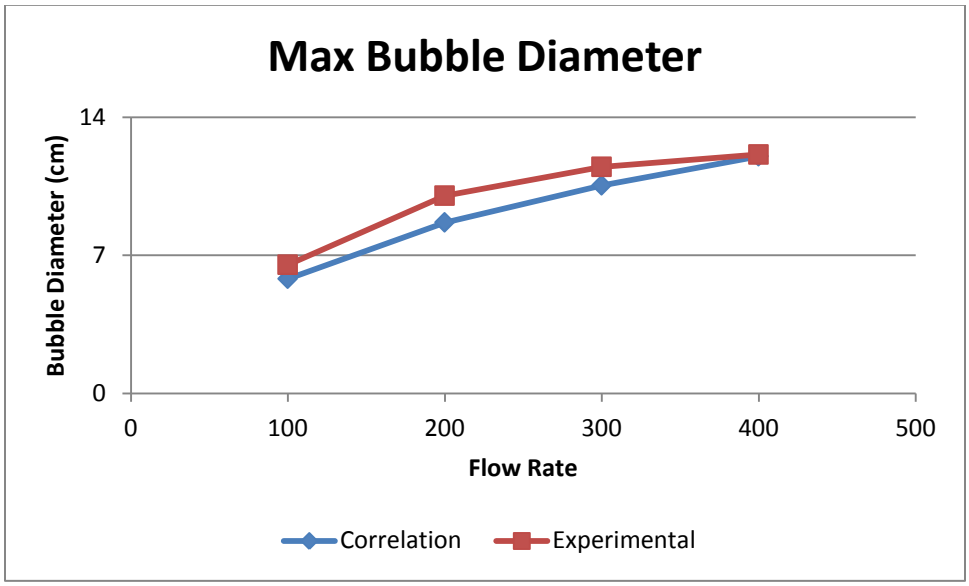

Figure 3.3. Comparison of combined mean experimental diameter with theoretical bubble diameter using Mori and Wen correlation (1991).

Figure 3.4 shows normalized bubble diameter frequency distribution for the two static heights with respect to air flow rates. When the bubble-to-bed diameter ratio (d_B/d_t) is greater than 0.6, the bed is in transitioning mode from bubbling to slugging (Kunni and Levenspiel, 1991). With this threshold the bed is in bubbling regime for both bed heights at the lowest flow rate of 100 LPM. At 200 LPM bubbles coexist with slugs indicating a transition. As the flow rates are increased further slug are the dominant mode of gas transfer and the beds are in hybrid bubbling-slugging regime.

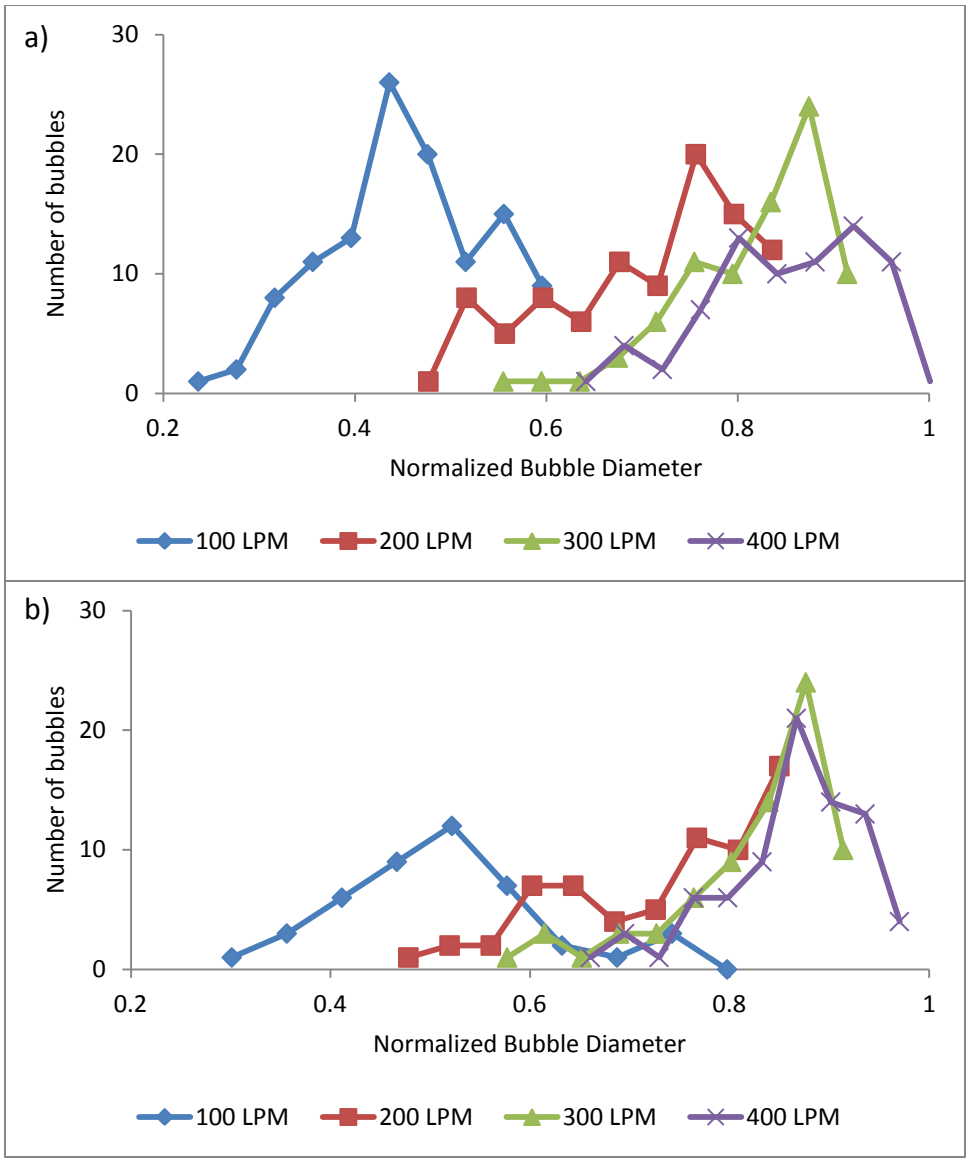

Figure 3.4. Normalized void diameter distribution in the a) 42 cm and b) 49 cm beds. The x-axis represents the normalized bubble diameter in an experimental run. The threshold value represents 60 % (8.4 cm) of the bed diameter.

3.1.2 Bubble Rise Velocity

Bubble rise velocity is an important hydrodynamic parameter of interest. The experimental bubble rise velocities will be compared to Davidson's rise velocity correlation. The bubble rise velocity in the bed can be estimated by:

$$U_b = (U_o - U_{mf}) + U_{br}, \quad (3.4)$$

where U_b is the average bubble rise velocity in the bed, U_O is the inlet gas velocity, U_{mf} is the minimum fluidization velocity and U_{br} is the rise velocity of a single bubble given by the following equation:

$$U_{br} = 0.711(gd_b)^{\frac{1}{2}}, \quad (3.5)$$

where d_b is the mean bubble diameter. The average bubble rise velocity obtained by applying DIAT to ECT data is given in Figure 3.5. The bubble rise velocity portrays a linear relationship as the superficial gas flow rate increases initially. A similar relationship but with lower velocity magnitudes was obtained in another study (Makkawi, 2002). This linearity is due to the smaller range of gas flow rates and as the air flow is increased the bed moves into bubbling-slugging regimes indicated by decreasing velocity. The increase in velocity of the shallow bed at 400 LPM can be attributed to increased turbulence and a wider range of bubbles with some moving faster than the rest on average. The mean bubble rise velocity is used for design calculations but as with bubble diameter a wide range of rise velocities have been detected in the bed.

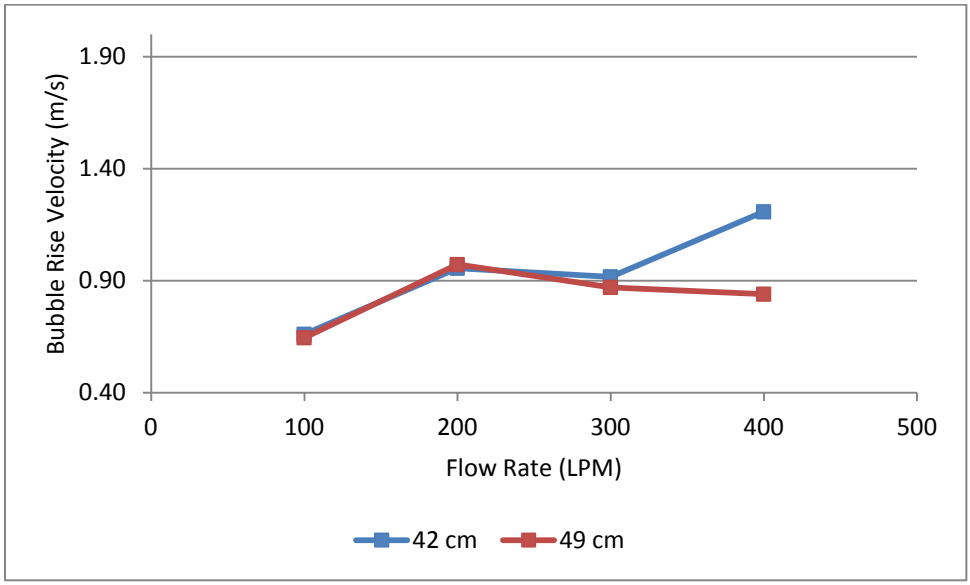

Figure 3.5. Average bubble rise velocity for the two bed heights with respect to flow rate.

A review of literature pertaining to bubble rise velocity and diameter suggest that studies tend to deal with mean values rather than distributions and their implications on bed behaviour if any. The bubble rise velocity distribution for static bed heights of 42 cm and 49 cm are shown in Figure 3.6. One can observe that there is a wide distribution of bubble rise velocities even though the mean rise velocities for all operating conditions are less than 1.2 m/s. Approximately 10-15 fast moving bubbles of higher magnitude outliers have not been shown in order increase the figure's visibility. The reviewed literature is void as to why such a large velocity distribution exists.

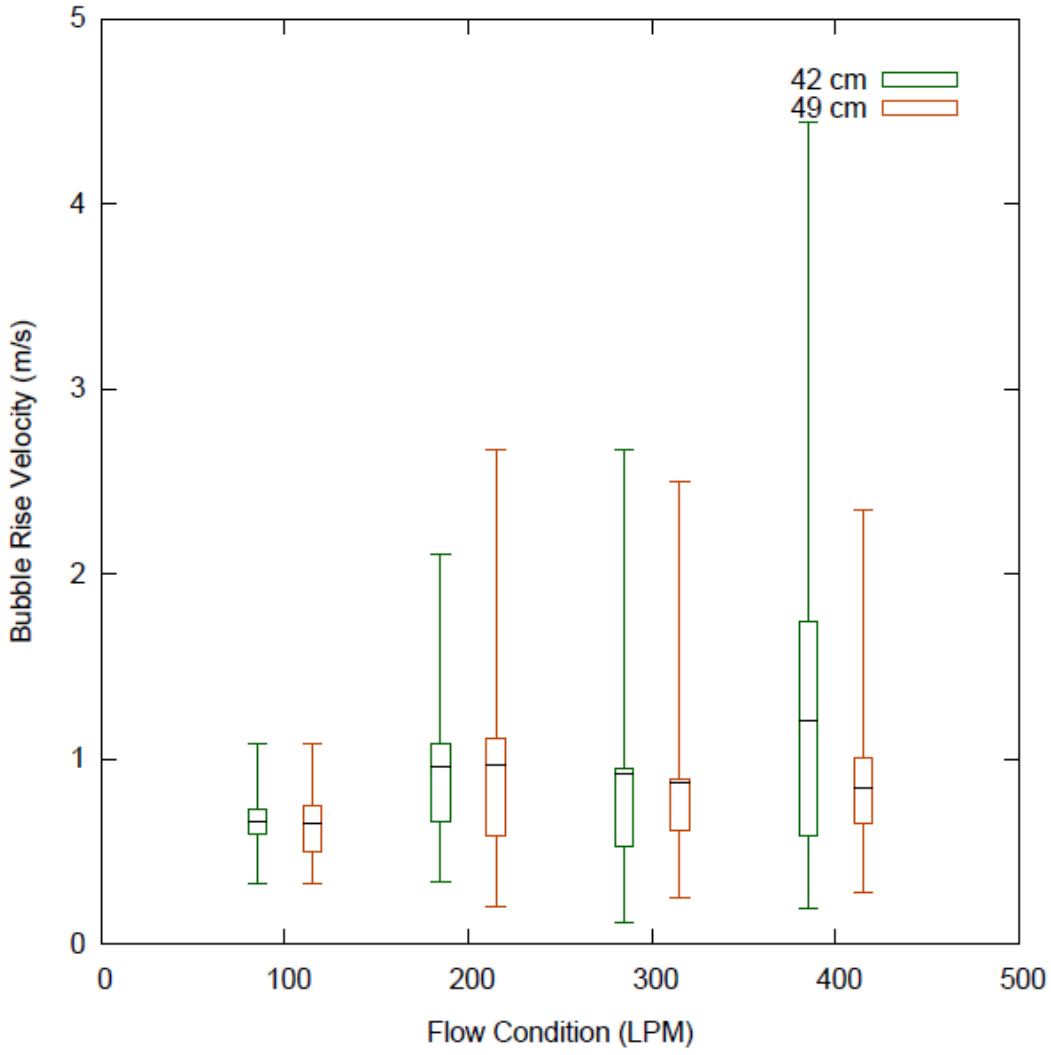

Figure 3.6. Distribution of bubble rise velocity in a bed of sand for two static bed heights of 42 cm and 49 cm at air inflow of 100, 200, 300 and 400 LPM respectively. The box represent the 25th percentile, mean and 75th percentile of bubble velocity. The extreme ends of the error bar represents minimum and maximum bubble rise velocity.

Traditionally the bubble rise velocity from electrical capacitance tomography systems is calculated from solid fraction time signals of the two planes. The comparison of rise velocities obtained from application of DIAT and solid fraction signals for static bed heights of 42 cm and 49 cm is given in Figure 3.7. The two techniques yield more-or-less the same results. The slight difference between the two can be attributed to different nature of the signals and post processing steps. On a frame-by-frame basis the solid fraction signal is

relatively smooth because it is an average value of a 32 x 32 matrix. Other the other hand the area of bubble diameter is a dynamic quantity and is constantly changing due to bed effects such as wall interaction and inter-bubble interaction. However without the inclusion of the velocity-diameter pair outliers, the signal yields different results as described in preceding pages.

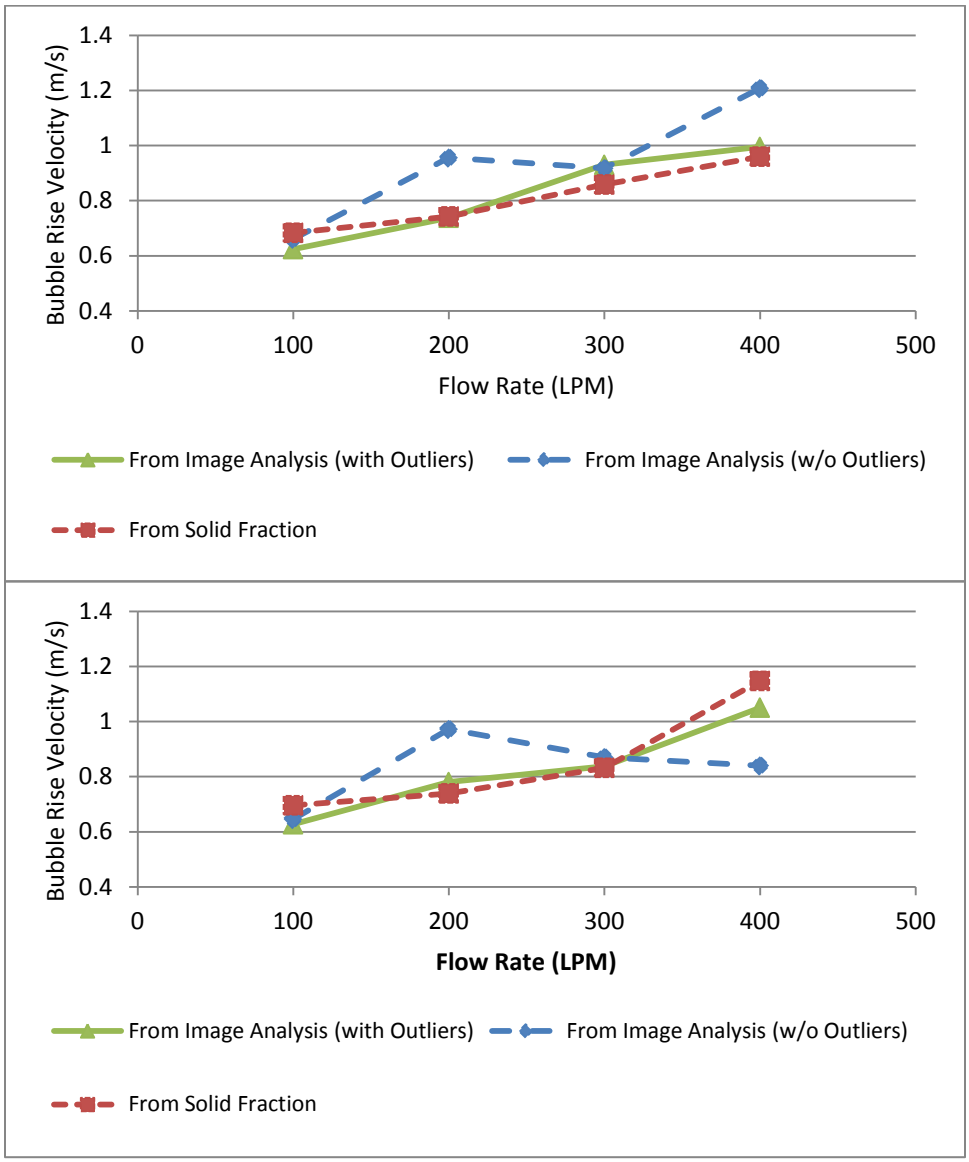

Figure 3.7. Comparison of mean bubble rise velocities at two bed heights a) 42 cm b) 49 cm as determined by Image analysis and Solid-fraction methods.

It is important to know how well bubble rise velocities compare to correlations given in literature. Based on the bubble diameter results it can be safely assumed that the fluidized bed moves from a bubbling to a bubbling-slugging hybrid regime between 200 LPM and 300 LPM. Therefore it is hard to choose a rise velocity correlation that predicts velocities across different regimes. Figure 3.8 compares the experimental mean bubble rise velocities obtained from the application of DIAT with velocities obtained from Davidson's correlation. The rise velocities for the two bed heights have similar values because 1) they are measured at the same height above the distributor 2) the minimum rise velocities are similar for both beds (see Figure 3.6). The minimal difference between the experimental velocities and Davidson velocities can be attributed to smaller range of experimental flow rates; an increase in air flow might lead to a significant difference between the two velocities. The mean minimum velocity for the two bed heights stays more or less similar indicating a lower velocity limit for this experimental set-up. However, the maximum bubble rise velocity increases in a linear fashion. This increase can be attributed to complex bed behavior such as interaction between the bubbles and a large diameter voids rising at higher velocities. The curve will level out once slugging has set in and the bed has transitioned to the slugging regime (Makkawi, 2002).

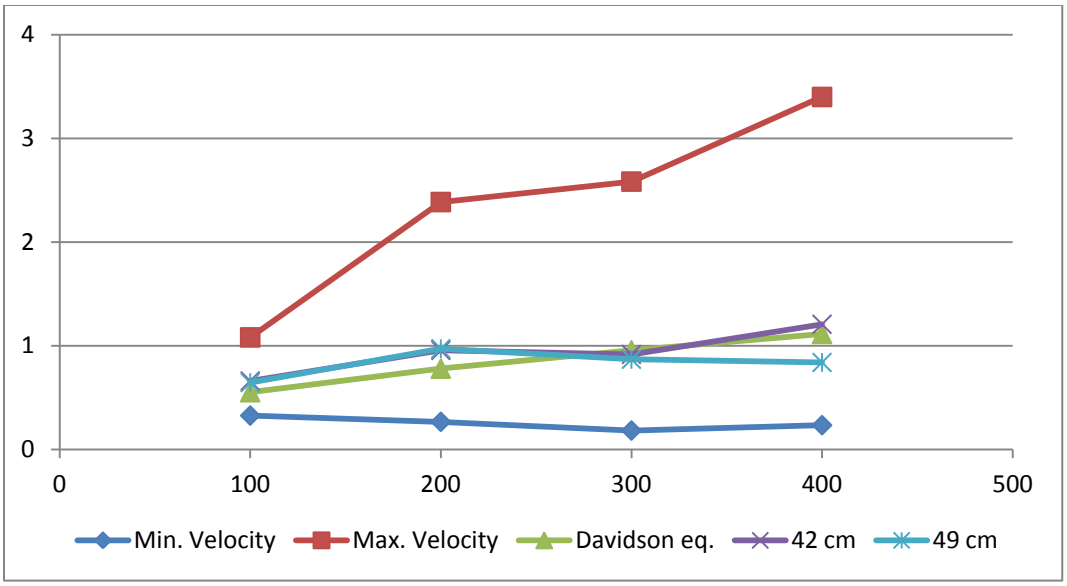

Figure 3.8. Comparison of theoretical bubble rise velocity (Davidson, 1991) with experimental means at 42 and 49 cm. Overall experimental maximum and minimum rise velocities for each flow rate are shown to demonstrated spread in data not captured by the Davidson correlation.

The bubble diameter and rise velocity have been discussed separately in the last two sections but it is important to see how these two parameters relate to each other. This parameter has not been studied utilizing ECT solid fraction measurements as far the studied literature is concerned. Bubbles formed in beds with Geldart B particles tend to grow with increased gas velocity. These values were compared to theoretical values obtained via equation (3.4) and are shown in Figure 3.9. The experimental values were obtained by taking the average of experimental velocities and experimental diameters for the two bed heights. The quasi bubbling/slugging regime is responsible for the difference between the experimental and theoretical results. The theoretical velocity obtained from eq. 3.4 is rising in a quasi linear fashion with the increase in bubble diameter but this trend is not seen for experimental results. The presence of slow moving slugs at flow rates of greater than 100 LPM tend to shift the data towards larger bubbles but with slower rise velocities.

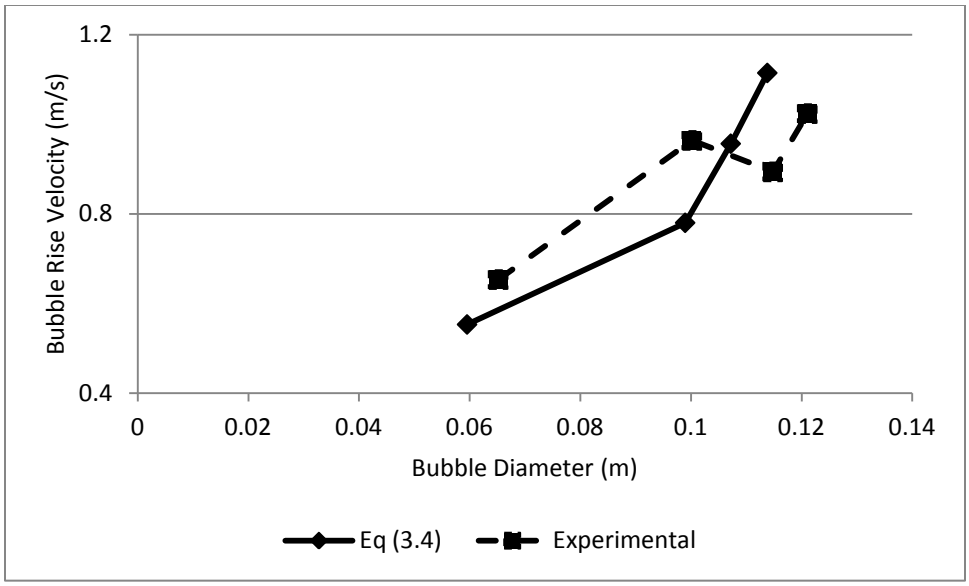

Figure 3.9. Comparison of combined bubble rise velocities versus bubble diameter at two bed heights with Davidson correlation (eq. 3.4).

There exists an operating envelope within which all the void diameter-velocity pairs exist for a particular flow condition. The envelope shows the minimum and maximum bubble diameter along with the corresponding velocity range for that air flow rate. Figure 3.10 illustrates that shallow bed's parameters divide the bed into two regions; one dominated by the lower flow rates and the one on right hand side where medium to high flow rates overlap. As the flow is increased smaller bubbles cease to exist and replaced with slugs. A further increase in flow takes the bubble size to bed diameter. Figure 3.11 illustrates the envelope for the deeper bed which differs from the shallow bed. The diameter-velocity envelope for 100 LPM overlaps the slugging regions unlike in the shallow bed. At 200 LPM the bed is in transition mode between bubbling and slugging. As the inlet gas flow rates are increased the beds moves into a transition bubbling-slugging mode. The envelopes indicate that slugging is more dominant in deeper beds even though it has not fully set in. This is the onset of slugging behaviour, however for a complete transition to slugging behavior a static bed height of 95 cm is required for a 14 cm diameter fluidized bed (Kunii and Levenspiel,

1991). Similar results were obtained in narrow beds of 0.05 m and 0.10 m diameter when slugs were introduced without complete transition (Du et al., 2005).

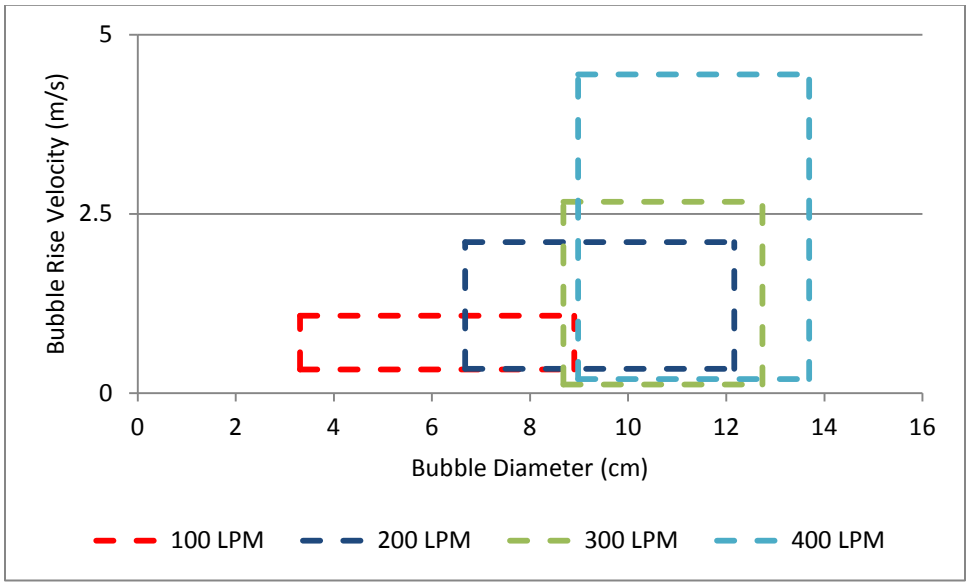

Figure 3.10. Bubble velocity envelope for a 42 cm bed. The corners of each box represent the extreme value pairs of bubble rise velocity and bubble diameter for a particular inlet gas flow rate.

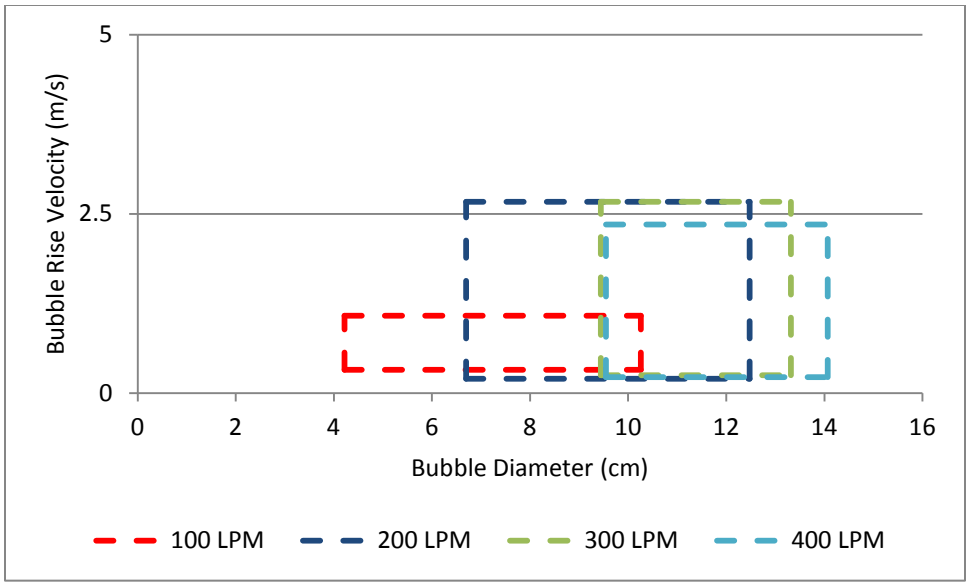

Figure 3.11. Bubble velocity envelope for a 49 cm bed. The corners of each box represent the extreme value pairs of bubble rise velocity and bubble diameter for a particular inlet gas flow rate.

3.2 Bed Behaviour

A wide variety of phenomena in fluidized beds such as gas-solid distribution, dynamics of two phase interaction, bed expansion and the bed operating regime are categorized as bed behaviour. Electrical Capacitance Tomography (ECT) provides a visual and quantitative distribution of the two phases. Digital Imaging Analysis (DIAT) previously applied to fluidization to study bubble properties and behaviour in two dimensional beds (Asegehegn et al., 2011; Agarwal et al., 1997). As far the author is aware these techniques have not been combined to study fluidized bed systems. The results of application of DIAT to ECT tomograms for bed behavior shall be discussed in successive sections.

3.2.1 General Bubble Behaviour

Bubbles in a fluidized bed behave in a dynamic manner; their size and structure changes as they rise up. ECT measurements were taken at a frequency of 100 Hz for an average measurement span of 50 seconds. These frame by-frame measurements formed the basis of analyzing bubble properties and bed behaviour. Bubble parameters such as area,

diameter, radial position and eccentricity were calculated for every frame. Beyond minimum bubbling conditions, the bubbles are present in the bed at all times but they take a finite amount of time to reach the measurement plane. Therefore a large number of frames had no voids in them, especially at low flow rates. The number of frames with a single void was much larger than the number of frames with multiple voids. Parameters such as bubble area and diameter for frames with multiple objects were calculated by taking the weighted average of individual voids to compute data and derive conclusions. The weighted average was calculated using the following equation:

$$x = \sum_{i=1}^{n} \left(\left(\frac{x_i}{\sum x_i} \right) \right) x_i \tag{3.6}$$

Where x is the parameter of interest such as area, i is the void number and n is the total number of voids in a frame.

The presence of multiple voids in a frame indicates the presence of multiple bubbles on the same radial plane, a single bubble breaking apart/joining up or the trailing lobes of bubble's bottom part. Figure 3.12 illustrates the three cases showing frames with multiple voids and their respective two-dimensional sketches in bed as captured by ECT and processed via application of DIAT. The frame number increases from top to bottom and then from left to right.

The first column shows two separate bubbles travelling in the same radial plane with the void on the left preceding the void on the right. The voids do not connect with each other while they cross at the measurement plane. This sort of behaviour is observed at low flow rates where bubbles do not interact among themselves owing to less turbulence in the bed. The second column shows two separate voids appearing in the same plane, then coalescing and subsequently parting ways shortly afterwards. The voids do not interact afterwards but as they move upwards their shape changes eventually erupting at the beds surface. This behaviour is observed at medium to high flow rates. Quasi-circular voids are shown in column (c), as the bubble rises circular voids are transformed into doughnut shapes due to

presence of an air cavity. The last three frames showing two separate voids are two dimensional representation of the bottom concave portion of the bubble and trailing lobes.

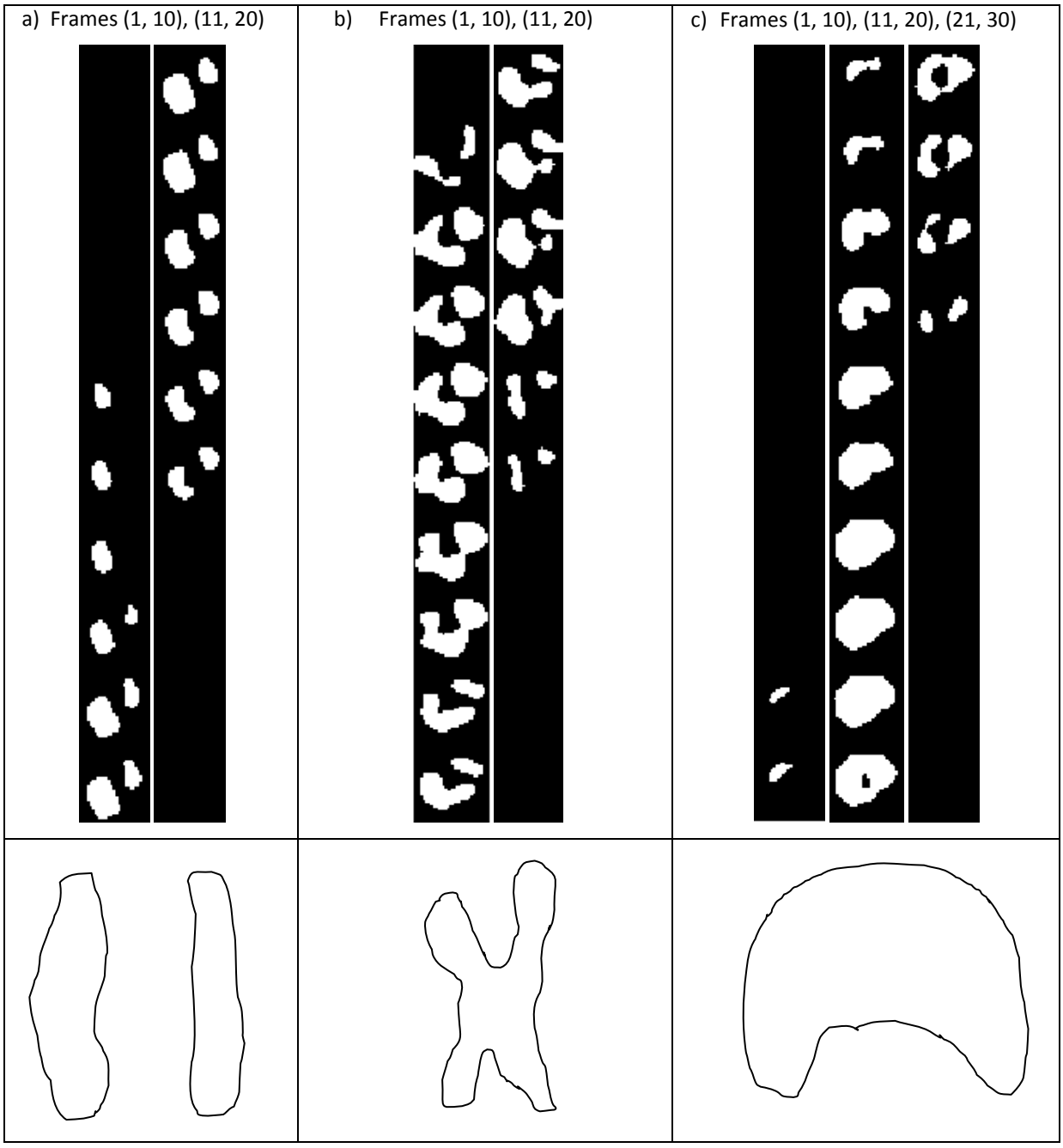

Figure 3.12. Different types of multiple voids in a frame. a) Two separate voids b) Elongated bubble with concave top and bottom c) Single spherical bubble with concave bottom. The images at the top show series of binary image voids constituting a bubble. The bottom sketches are author's reconstruction of the voids.

The presence of multiple voids can indirectly indicate the character of the bed and can potentially show bubble activity in the bed. It is important to note that each frame represents a two dimensional slice of a bubble not the bubble itself. This complicates the discussion because multiple voids were obtained for all three cases sketched in Figure 3.12. However generic conclusions can be described by looking at the multi-void frames. The two bed heights show opposite behavior with respect to presence of multi-void frames. Figure 3.13 shows the percentage of number of multi-void frames with respect to total number of frames with voids. For the shallow 42 cm bed, the numbers of multi-void frames stays constant at around 10%. On the other hand the 49 cm bed has more multi-void frames at lower flow rates and then as the inlet flow rate increases the number decreases. There is a bed height effect that is impacting the bed behavior. Conclusion about bed behavior cannot be pinpointed based on the number of multi-void frames but rather is a general indicator that bed behavior is changing at a given condition. It has been mentioned that previously that slugging should not completely set in at bed height of less than 95 cm. The shallow 42 cm bed does not exhibit a change in number of multi-void frames indicating 1) the average bubble size is smaller indicating smaller bottom bubble lobes and 2) significant presence of bubbles along with slugs. For the deeper 49 cm bed the decrease can be attributed to the disappearance of smaller multiple voids being replaced by slugs. However, this is a generic indication of bed and bubble behaviour; specific conclusions like when or why is this change happening cannot be based on this particular information.

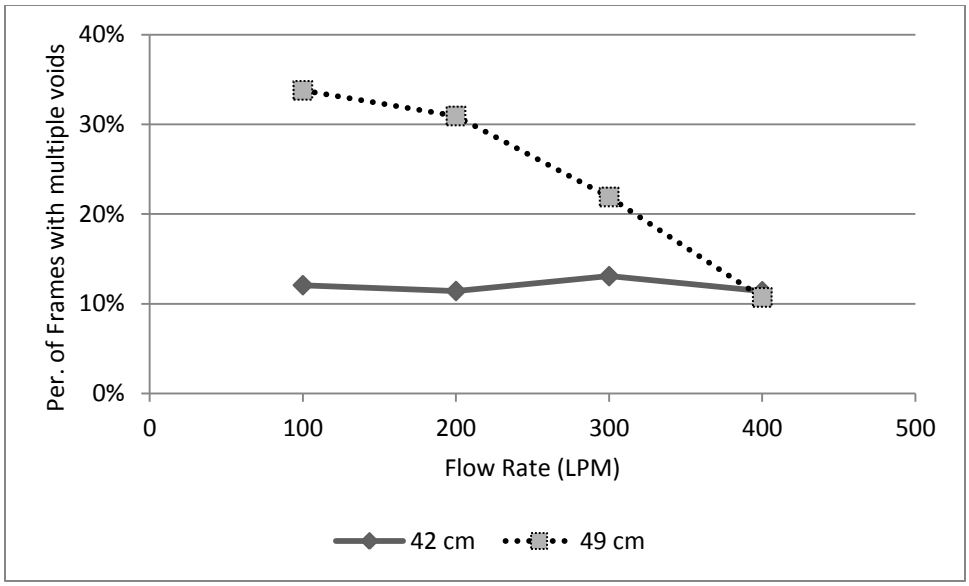

Figure 3.13. Normalized number of multi-void frames versus flow rate.

3.2.1.1 Eccentricity

Eccentricity is a measure of how much a shape deviates from a perfect circle, with 0 being a perfect circle and 1 being a straight line. The author could not find any precedent of defining bubble eccentricity or whether it can yield any information regarding bed behavior using ECT measurements. In two-dimensional beds aspect ratio is a parameter that is similar to eccentricity but with major difference. Aspect ratio is the ratio of extreme vertical to horizontal distance measured from the side. In this research eccentricity of voids was measured from binary images using MATLAB's build-in function for the all voids for every flow condition. Eccentricity is defined as the ratio of the distance between the ellipse's foci and the major axis length. The corresponding ellipse is constructed around the void and the corresponding eccentricity is calculated. Figure 3.14 shows a passing bubble and its two-dimensional cross-section and eccentricity value of every frame. The eccentricity of two voids in a single frame was calculated by taking the weighted average of the two voids. The eccentricity of a bubble changes significantly as it passes the sensing planes.

The eccentricity distribution of voids for all experimental conditions is shown in Figure 3.15. Eccentricity of all voids was used instead of using the eccentricity of a single largest void.

The maximum and minimum eccentricity limits are similar for the both bed heights. The general behavior indicates that eccentricity of individual voids decreases, that is they become more circular, as the inlet air flow rate is increased. The average eccentricity for the shallow bed decreases and stabilizes at 0.65 for flow rates greater than 200 LPM. As the bubbles become large with increased air flow they tend to reach an average diameter of 11 cm for the given flow conditions. The deeper 49 cm bed exhibits a different behavior; the eccentricity of the voids decrease with the increasing inlet flow rates. This behavior can be attributed to presence of bed-sized slugs which tend to be circular in nature. The eccentricity of voids indicates that the bubbles are not circular in nature when viewed from the top. This complements the study conducted by Asegehegn et al. (2011), where the bubbles were found to be less circular at bed height of 0.4 m.

Void	Eccentricity	Void	Eccentricity	Void	Eccentricity
	0		0.52		0.89
	0		0.45		0.89
	0		0.40		0.89
	0		0.40		0.88
	0.73		0.36		0.88
	0.80		0.32		0.86
	0.78		0.31		0.77
	0.79		0.28		0.55
	0.70		0.24		0.58
	0.61		0.21		0.82

Figure 3.14. Frame-by-frame changes in eccentricity of a bubble passing a sensor plane.

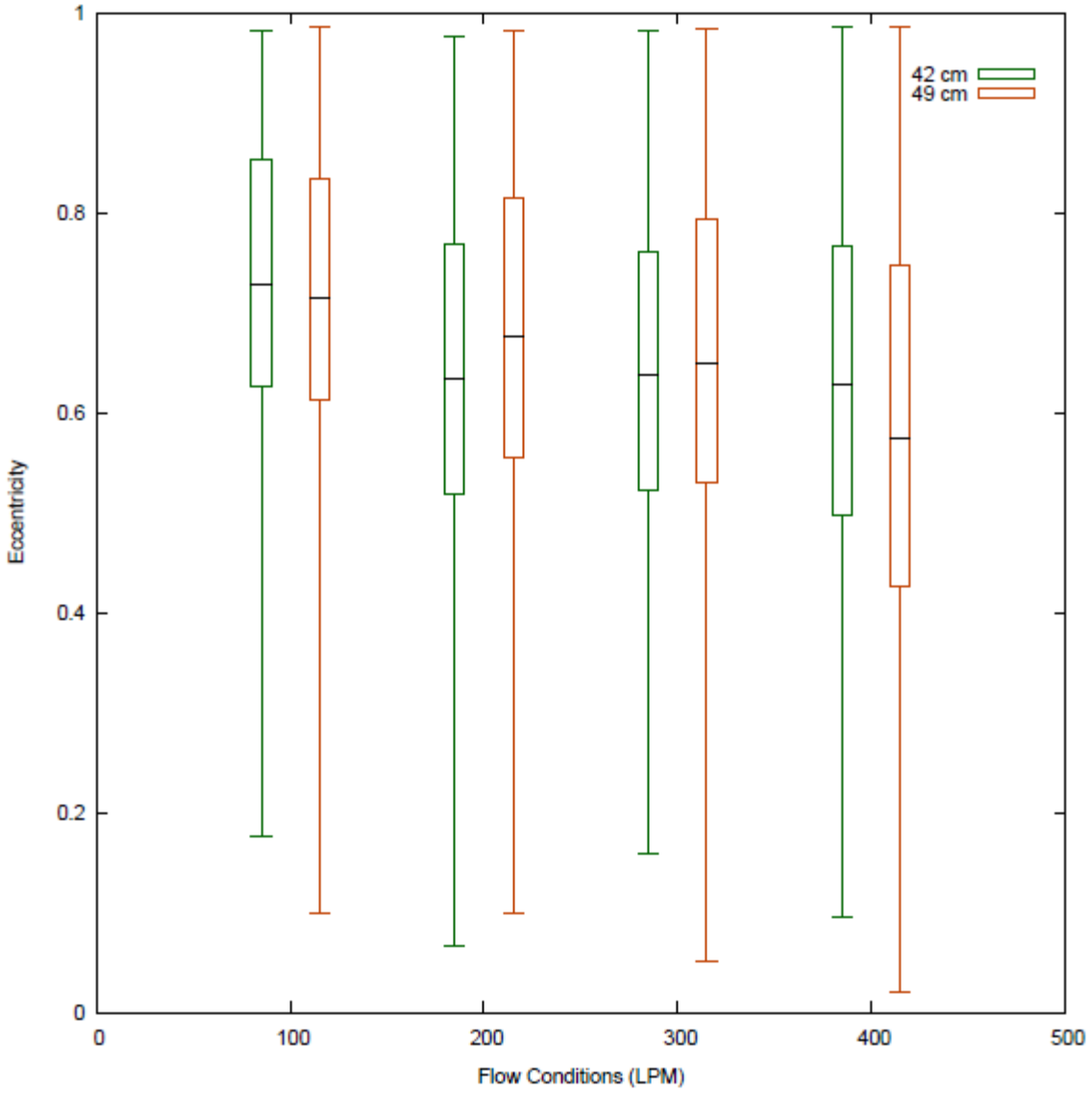

Figure 3.15. Distribution of eccentricity of individual voids for static bed heights. The box represent the 25th percentile, mean and 75th percentile of eccentricity. The extreme ends of the error bar represents minimum and maximum void eccentricity.

3.2.2 Gas-Solid Distribution

Gas-solid distribution is an important parameter for fluidized bed design and operations. Uniform two-phase distribution is essential for avoiding hot spots in the fluidized bed reactors, achieving higher reactant conversion, increasing heat and mass transfer rates in the reactor. To achieve these goals different types of reactor internals are installed in

fluidized beds to control the two-phase distribution (Yang and Peng, 2003). Optical fibre and pressure sensor probes have been used to measure the gas-solid distribution in beds (Du and Warsito, 2003; Pugsley et al., 2003). The average solid fraction in the bed for an experimental run was obtained by averaging the solid fraction of approximately 5000 frames into a single frame. The "average frame" was used to obtain the radial solid fraction by taking the mean of solid fraction of the middle rows and columns. Figure 3.16 highlights the middle rows and columns (16 and 17) in a 32 x 32 matrix.

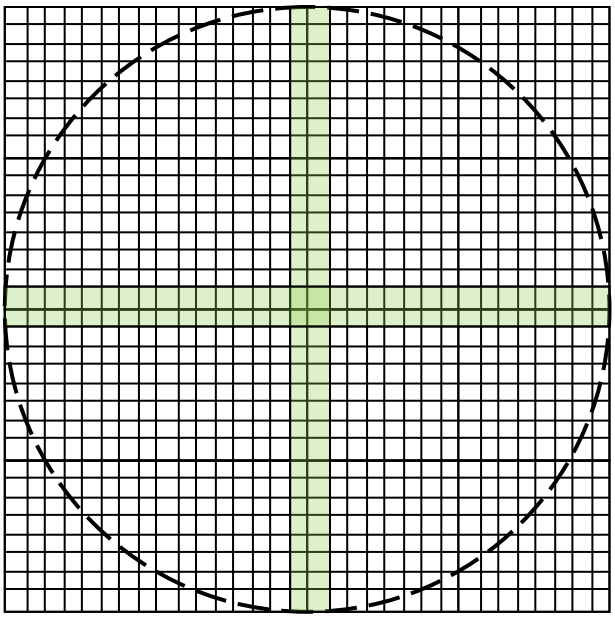

Figure 3.16. Pixels (shaded) utilized to determine average solid radial distribution.

The average radial solid fraction distribution representing approximately 5000 frames for the two bed heights is given in Figure 3.17. It is interesting that bed height seems to have relatively little effect on the average values of solid fraction. The solid fraction for a bed height of 49 cm is more symmetric and seems to have an inverted "M" profile for all flow conditions. For the shallow 42 cm bed "M" profile is visible for the two higher flow rates

indicating transition to slugging regime. The “M” profile has been associated with transition from bubbling to turbulent regime for dry pharmaceutical granules (Weins and Pugsley, 2006).

The maximum solid fraction in Figure 3.17 lies at the outer periphery of the bed with a local maxima just around the bed’s center. This indicates that on average the bubbles do not rise through the outer regions. Their preferred path of rise lies around the bed’s center at the half way point at r/R of -0.5 and 0.5 indicated by lower solid fraction. The local solid fraction peak at the bed’s center is due to accumulation of solids in front the bubble as it rises. As bubbles rise they displace solid particles in their path resulting in an increased local solid fraction at the bed’s edges. After the bubbles have passed the sensing plane the solid particles fall back into their original position. They are joined by additional solid particles thus increasing the local solid fraction thus giving way to higher solid fraction at the bed’s centre and outer periphery.

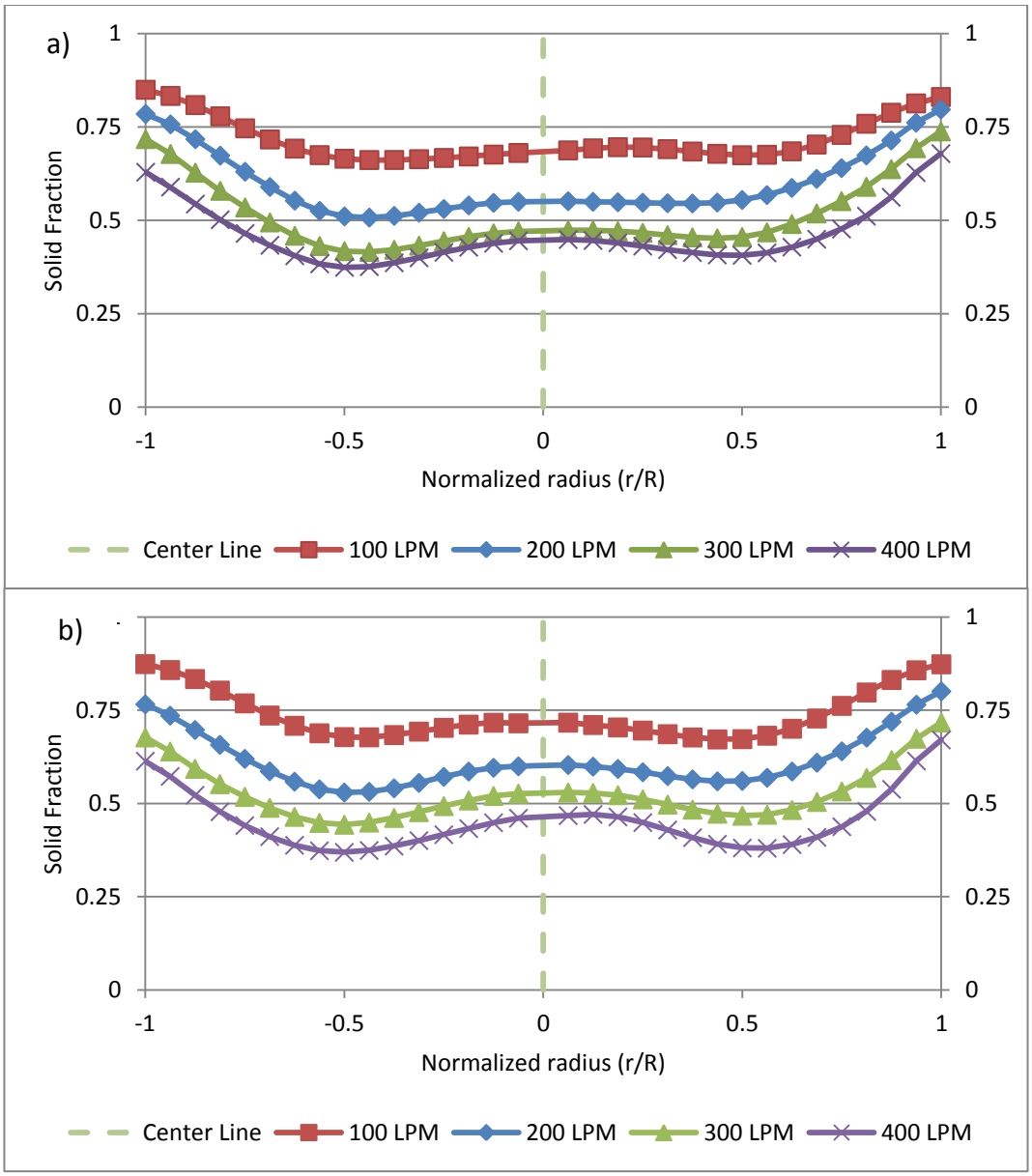

Figure 3.17. Radial solid fraction profile at bed heights of a) 42 cm b) 49 cm at four inlet flow rates.

The average solid fraction distribution provides limited information regarding the position of bubbles and whether size is related to bubble's position in the bed. For larger sized beds it would be important to know that bubble's position as it rises in the bed. The bubble's position can have an impact on various aspects of chemical reaction and reactor operability. The position of bubbles in narrow beds can provide limited information because the

bubbles can grow to be as large as bed's diameter at higher air flow rates. However it is important to demonstrate how ECD with DIAT can yield bubble's position. This can be potentially useful to study the rise of gases and subsequent effect on solid concentration in different materials where bubbles are not mode of gas transportation. The radial positions of the bubbles were obtained by mapping the center of mass x and y coordinates. However, the center of mass coordinates for every void does not provides any useful information about bubble's position because of complex nature/shape of individual voids as shown in Figure 3.12. Hence, the bubble's position was represented by using the x-y coordinates of void with the largest area/diameter.

The center of mass for the void of maximum area for the two bed height at is shown in Figure 3.18 and Figure 3.19 respectively. The void with largest diameter was chosen to represent the bubble position at the measurement plane instead of plotting the position of all voids to avoid clutter and distract from obtaining meaningful conclusions. The size of the voids was normalized by the bed diameter and has been scale down by a factor of 10 for visualization purposes. The circle in the top right corner of the plots represents the largest possible bubble equivalent to the bed diameter scaled down for visualization.

For a bed height of 42 cm and gas flow rates of 100 LPM and 200 LPM the bubbles are distributed in a symmetric manner around the bed. However for the two higher air flow rates majority of bubbles rise up in the lower half of the plot. This uneven distribution is observed across vertical axis only and can be attributed to uneven floor, back and forth rocking of the fluidization bed apparatus. It is also worth noting that majority of bubbles in the region bounded between r/R of -0.5 and 0.5 on the horizontal axis. Larger bubbles generally tend to move in the central portion of the bed, while smaller bubbles travel in the middle to outer regions of the bed. The bubbles are more dispersed for both beds at gas flow rates of 100 LPM and 200 LPM. This is due to the smaller bubble size whose interaction such as bubble coalescing is much less frequent. Larger bubbles are formed as a result of increased air flow and coalescing of smaller bubble. As they rise up they move towards the central regions of the bed. An increase in gas flow take the bed into bubbling-slugging

regime where rising gas occupies the majority of bed's cross section and moving through the central region. The observation complements the results obtained from solid fraction distribution that the bubbles congregate in the central portion of the bed especially at higher flow rates.

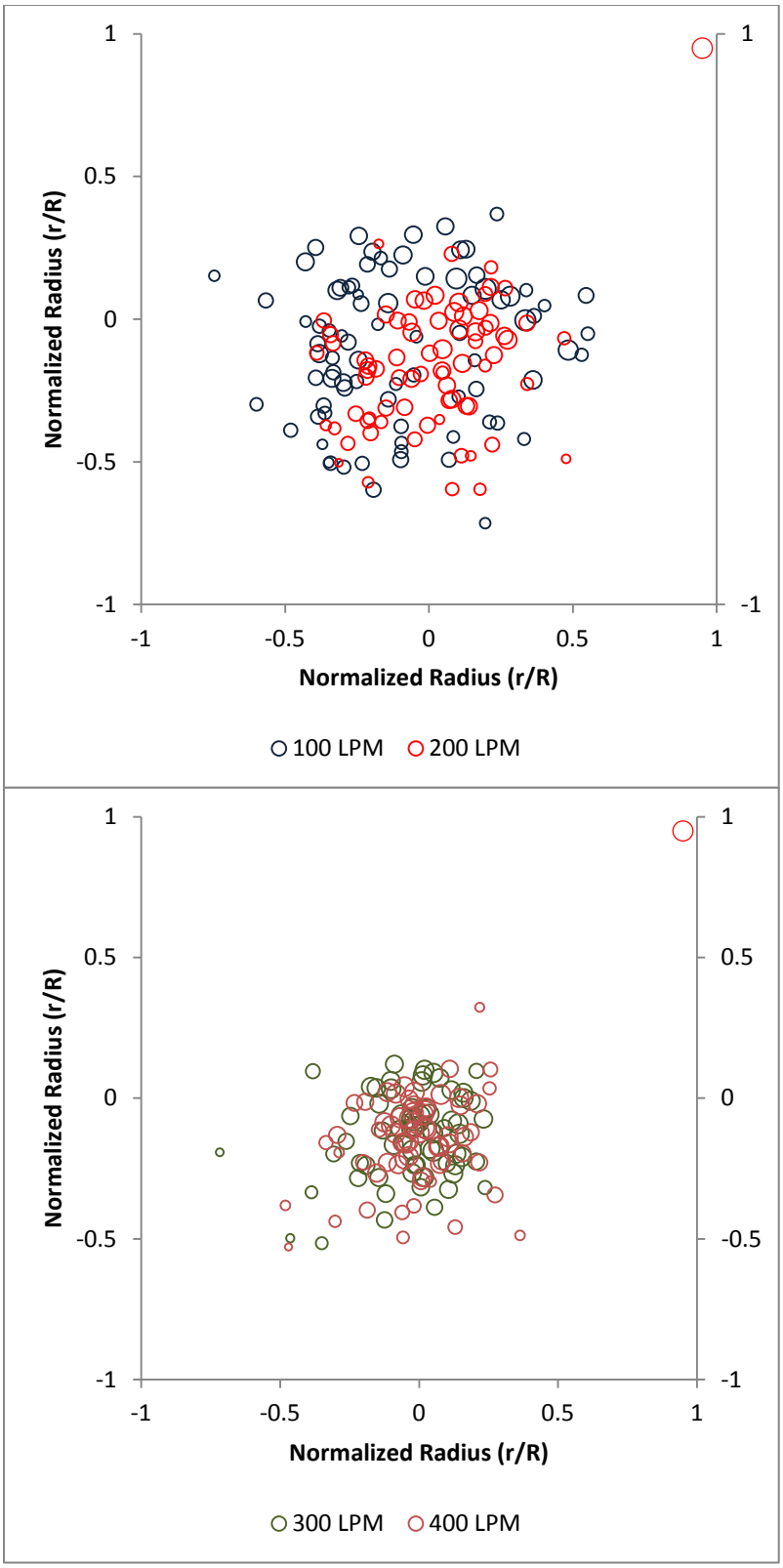

Figure 3.18. Bubble position in a 42 cm bed. The circle in top right represents a void with similar size as bed size.

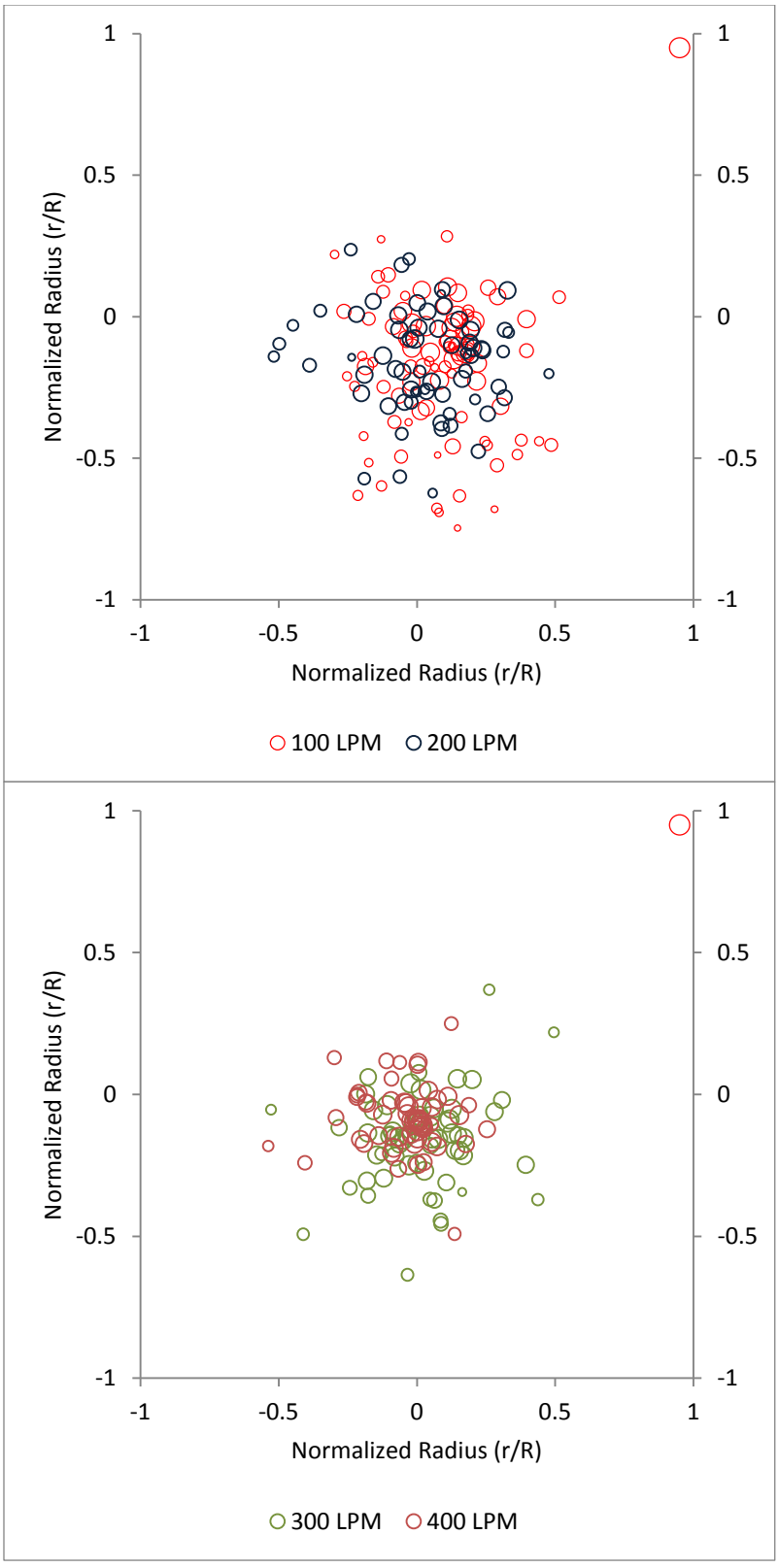

Figure 3.19. Bubble position in a 49 cm bed. The circle in top right represents a void with similar size as bed size.

3.3 Distinct Bubble Shapes

The measurement of solid fraction in fluidized beds can provide a quantitative overview of hydrodynamic properties of the bed. Bubble behavior can be isolated and studied by delineating the gas-solid boundary. The binary images further discern the bubbles for solid fraction showing that the bubbles are far from ideal and come in all shapes and sizes. They are dynamic objects very susceptible to changes when subjected to different process conditions. It is important to know the distinct bubble behavior in the bed as they can have a significant impact on the fluidization process. It is important to state that these bubbles were not observed directly but were inferred from the binary images which themselves were obtained from solid fraction distribution maps. The frames constituting the various bubble types are shown in Figure 3.20, with bubbles starting from left to right and top to bottom. For the purpose of this thesis the following five bubble behaviors were inferred:

i. Spherical Bubble: These bubbles have been observed at low flow rates (100 LPM and 200 LPM) and are shaped in a spherical manner; two-dimensional voids are shaped in a circular manner slices consist of spherical shaped smaller circular voids.
ii. Regular Bubble: These are typical bubbles observed for Geldart A and B particles. They exist in bubbling fluidized beds and consist of a top spherical portion. The bottom portion consists of low pressure concave area with a doughnut like structure appearing in last couple of frames.
iii. Incomplete/Crescent Bubbles: These bubbles consist of irregular shaped voids. The voids are crescent shaped with solids penetrating from one side of the bubble resembling a half doughnut. The existence of these non-spherical bubbles can't be explained precisely.
iv. Slugs: These air cavities cover most of the bed's cross section area and exist mainly at higher flow rates of 300 LPM and 400 LPM. The corresponding voids are quasi circular in shape or be irregular in shape.
v. Splitting Bubble: Bubbles often split when a gas wedge is formed and inward solid moment leads to bubble splitting. This behaviour was not commonly observed and took place at medium to high flow rates due to increased bed disturbance.

Bubble Type	Void Images
i) Spherical	
ii) Regular	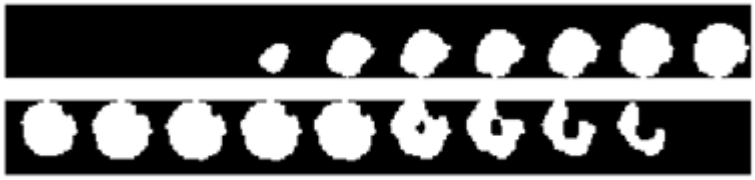
iii) Incomplete	
iv) Slugs	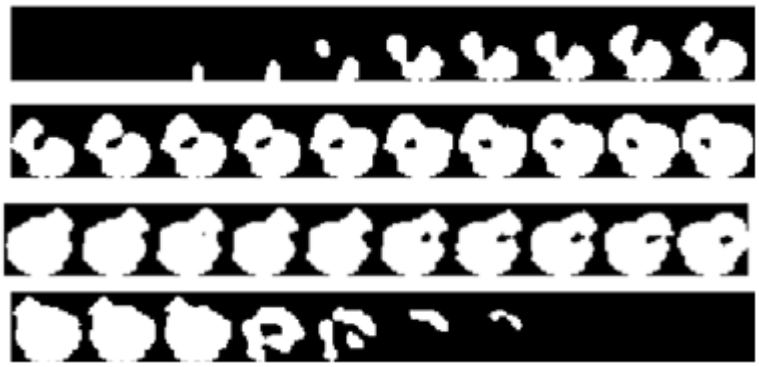
v) Splitting	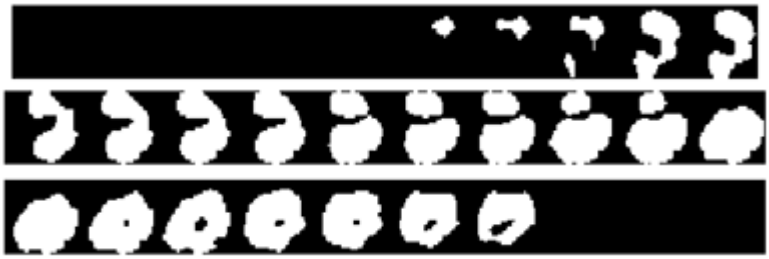

Figure 3.20. Binary images of various void types.

3.4 Limitations of the Experimental Technique

Many techniques have been devised to determine the complex bubble behaviour in a fluidized bed. ECT describes the relative fraction of two dielectric materials in a fluidized

bed, while DIAT is used to study bubble phase mostly in two-dimensional beds. However it is important to know the limitations and shortcomings of a measurement technique to properly reach meaningful conclusions. In the course of research the following limitations have been identified:

1. This technique relies on ECT data hence the fundamental limitations of ECT are directly transferred to ECD plus DIAT. These include low resolution of ECT, the accuracy of reconstruction of bed's behavior, and the local nature of measurement.
2. Determining the solid-bubble boundary is any important preliminary step before bubble behaviour can be discerned. The solid-bubble boundary might differ for various bed materials hence it is difficult to automatically determine the boundary. An incorrect bubble boundary will distort the bed's picture and will be unable to capture correct bed behaviour.
3. The conversion of solid fraction tomograms to binary images and then obtaining useful information is regime limited. As the inlet gas flow rate is increased, the bed moves from bubbling to slugging then on to turbulent regime. The transition from bubbling to turbulent regime is characterized by a peak in standard deviation of solid fraction curve followed by a decrease in standard deviation eventually levelling off indicating fast fluidization. The slugs occupying large cross sections of the bed break up due to further inflow of gas making way for multiple bubbles. Additional inflow of gas causes the solid-gas boundary to diminish paving way for channels of gas moving up the bed. These channels will not behave like bubbles and different analysis techniques would be required to obtain useful information.

4 Conclusions and Recommendations

A new technique was devised to study fluidized bed hydrodynamic in a 14 cm diameter acrylic vessel using non-intrusive Electrical Capacitance Tomography (ECT) and applying a component of Digital Image Analysis Technique (DIAT). This was an attempt to combine two existing techniques to provide a better insight into fluidized bed behavior and check the utility of using ECT to study the gaseous phase. Sand was used as the fluidizing material at two static bed heights of 42 cm and 49 cm with gas flow rates of 100 LPM, 200 LPM 300 LPM and 400 LPM. The experiments were conducted for a span of 50 seconds with a measurement frequency of 100 Hz. The gas-solid distribution obtained from ECT formed the basis of hydrodynamic analysis. The bubble boundary was defined to a gas-solid fraction of 0.25. Hydrodynamic parameters such as bubble diameter and rise velocity were determined along with their distribution in the bed. Both the bubble diameter and their rise velocity were independently tested to verify ECT's ability to measure them. The results demonstrate that these two measurement techniques can be combined to provide a better insight into fluidized bed behavior. The following conclusions are based on research conducted:

1. The average bubble diameter for both bed heights is similar and agrees well with established correlations for Geldart B particles. However, the standard deviation of bubble diameter shows a different behaviour for the two beds. The standard deviation increases for the shallow bed and decreases for the deeper bed. This is due to the presence of slugs occupying large sections of bed's cross section area. Smaller bubbles are present along with the slugs in shallow bed thus increasing the standard deviation however slugs dominate the bed behaviour in deeper bed reducing the spread.
2. Bubble rise velocities calculated from the void area time series concur with velocities obtained from the solid fraction time series signal. The average experimental velocities were similar to the velocities obtained from the correlation but there was a large spread around the mean velocities.

3. Experimental bubble velocity was mapped as a function of experimental void diameter. For medium to high flows the bubble velocities and diameter overlapped each other indicating transition to slugging regime, unlike low flow conditions. The experimental velocities as a function of diameter were lower than the ones obtained from correlations because they deal with bubbles only instead of slugs and bubbles simultaneously.
4. Bubbles in bed rise through the midway point between the bed's center and inner edge. However, the individual bubbles are not spread out evenly in the bed. The majority of the bubbles rise through the lower two quadrants of the bed and concentrate in the center as inlet gas flow rate is increased.
5. Five different bubble types observed were i) Spherical ii) Regular iii) Irregular iv) Slugs and v) Splitting.

Based on results obtained the following recommendations are made:

1. Particles of different types such as FCC particles and petroleum coke should be fluidized to check the applicability of this technique to other particle types. The bed hydrodynamic behavior might differ and will also test the assumption regarding the definition of bubble boundary whether 0.25 will suffice for most particle types, or whether every particle type requires a different gas-solid boundary.
2. Reactor internals such as tube banks should be installed in ECT sensor to determine ECTs ability to capture hydrodynamic information in a reactor-like environment. This will also provide a novel opportunity to determine particle-tube behavior. Forces on tubes can be measured by this mechanism and be related to bubble properties in the bed.
3. Regimes beyond slugging need to be investigated through ECT plus DIAT to check this technique's ability to obtain useful hydrodynamic information beyond bubbling beds.

References

Agarwal, P.K., A.S. Hull and K.S. Lim, "Digital image analysis techniques for the study of bubbling fluidized beds," in "Non-invasive Monitoring of Multiphase Flows," J. Chaouki, F. Larachi and M. P. Dudukovic, Eds. Elsevier, Amsterdam (1997), pp. 407-422.

Asegehegn, T.W., M. Schreiber and H.J. Krautz, "Investigation of bubble behavior in fluidized beds with and without immersed horizontal tubes using a digital image analysis technique," Powder Technology. **210**, 248-260 (2011).

Bi, H.T., J.R. Grace, C.J. Lim and D. Rusnell, "Hydrodynamics of the Stripper Section of Fluid Cokers," Canadian Journal of Chemical Engineering. **83**, 161 (2005).

Busciglio, A., G. Vella and L. Rizzuti, "Analysis of the bubbling behaviour of 2D gas solid fluidized beds: Part II. Comparison between experiments and numerical simulations via Digital Image Analysis Technique," Chemical Engineering Journal. **148**, 145-163 (2009).

Caicedo, G.R., J.J.P. Marques, M.G. Ruiz and J.G. Soler, "A study on the behavior of bubbles of a 2D gas-solid fluidized bed using digital image analysis," Chemical Engineering and Processing: Process Intensification. **42**, 9-14 (2003).

Chaouki, J., F. Larachi and M.P. Duduković, "Noninvasive Tomographic and Velocimetric Monitoring of Multiphase Flows," Industrial and Engineering Chemical Research. **36**, 4476-4503 (1997).

Chaplin, G. and T. Pugsley, "Application of chaos analysis to pressure fluctuation data from a fluidized bed dryer containing pharmaceutical granule," Powder Technology. **142**, 110-120 (2004).

Chirone, R., F. Miccio and F. Scala, "Mechanism and prediction of bed agglomeration during fluidized bed combustion of a biomass fuel: Effect of the reactor scale," Chemical. Engineering. Journal. **123**, 71-80 (2006).

Clift, R. and J.R. Grace, "Continuous Bubbling and Slugging," in "Fluidization," J. F. Davidson, D. Harrison and R. Clift, Eds. Academic Press Inc., Orlando (1985).

Couderc, J., -P, "Incipient Fluidization and Particulate Systems," in "Fluidization," J. F. Davidson, R. Clift and D. Harrison, Eds. Academic Press Inc.., London (1985).

Davidson, J.F. and D. Harrison, "Fluidization Particles," Cambridge University Press, Cambridge. (1963).

Deen, N.G., W. Godlieb, S. Gorter and J.A.M. Kuipers, "An electrical capacitance tomography study of pressurized fluidized beds," The 13th International Conference on Fluidization. (2010).

Du, B., Q. Marashdeh, W. Warsito, A.-. Park and L.S. Fan, "Development of Electrical Capacitance Volume Tomography (ECVT) and Electrostatic Tomography (EST) for 3D Density Imaging of Fluidized Bed System," The 12th International Conference on Fluidization - New Horizons in Fluidization Engineering. (2007).

Du, B. and W. Warsito, "Bed non-homogeneity in turbulent gas-solid fluidization," AICHE Journal (USA). **49**, 1109-1126 (2003).

Du, B., W. Warsito and L. Fan, "ECT studies of gas-solid fluidization beds of different diameters," Industrial Engineering and Chemical Research. **44**, 5020-5030 (2005).

Ellis, N., H.T. Bi, C.J. Lim and J.R. Grace, "Hydrodynamics of turbulent fluidized beds of different diameter," Powder Technology. **141**, 121-136 (2004).

Geldart, D., "Types of gas fluidization," Powder Technology. **7**, 285 (1973).

Hull, A.S., Z. Chen, J.W. Fritz and P.K. Agarwal, "Influence of horizontal tube banks on the behavior of bubbling fluidized beds: 1. Bubble hydrodynamics," Powder Technology. **103**, 230-242 (1999).

Karimipour, S. and T. Pugsley, "A critical evaluation of literature correlations for predicting bubble size and velocity in gas–solid fluidized beds," Powder Technology. **205**, 1-14 (2011).

Kunii, D. and O. Levenspiel, "Bubbles in Dense Beds," in "Fluidization Engineering," John Wiley & Sons Inc., New York (1977), pp. 108-134.

Kunii, D. and O. Levenspiel, "Fluidization Engineering," Butterworth-Heinemann (1991).

Lim, K.S., J.X. Zhu and J.R. Grace, "Hydrodynamics of Gas-Solid Fluidization," International Journal of Multiphase Flow. **21**, 141-191 (1995).

Makkawi, Y.T., "Optimization of experiment span and data acquisition rate for reliable electrical capacitance tomography measurement in fluidization studies—a case study," Measurement Science and Technology. **13**, 1831-1841 (2002).

Makkawi, Y.T. and P.C. Wright, "Tomographic analysis of dry and semi-wet bed fluidization: the effect of small liquid loading and particle size on the bubbling behaviour," Chemical Engineering Science. **59**, 201–213 (2004).

Makkawi, Y.T. and P.C. Wright, "Fluidization regimes in a conventional fluidized bed characterized by means of electrical capacitance tomography," Chemical Engineering Science. **57**, 2411-2437 (2002).

Malcus, S., G. Chaplin and T. Pugsley, "The hydrodynamics of the high-density bottom zone in a CFB riser analyzed by means of electrical capacitance tomography (ECT)," Chemical Engineering Science. **55**, 4129-4138 (2000).

Marashdeh, Q., "ADVANCES IN ELECTRICAL CAPACITANCE TOMOGRAPHY," PhD Thesis, The Ohio State University. (2006).

Martin, M.P., P. Turlier, J.R. Bernard and G. Wild, "Gas and solid behavior in cracking circulating fludized beds," Powder Technology. **70**, 249-258 (1992).

Mckeen, T.R. and T.S. Pugsley, "The influence of permittivity models on phantom images obtained from electrical capacitance tomography," Measurement Science and Technology. **13**, 1822-1830 (2002).

Park, A.-. and L.-. Fan, "Fluidization," in "Encyclopedia of Chemical Processing," S. Lee, Ed. Taylor & Francis Group (2006), pp. 997-1007.

PTL, "ELECTRICAL TOMOGRAPHY SYSTEM TYPE PTL300-TP-G INSTRUCTION MANUAL," (1998).

Pugsley, T., H. Tanfara, S. Malcus, H. Cui, J. Chaouki and C. Winters, "Verification of fuidized bed electrical capacitance tomography measurements with a fibre optic probe," Chemical Engineering Science. **58**, 3923-3934 (2003).

Ramaswamy, S., M.J. McCarthy and R.L. Powell, "Pulp flow visualization using NMR imaging," in "Non-Invasive Monitoring of Multiphase Flows," Chaouki, J., Larachi, F., Dudukovic´, M. P., Ed. Elsevier, Amsterdam (1997), pp. 247-261.

Rimpiläinen, V., L.M. Heikkinen and M. Vauhkonen, "Moisture distribution and hydrodynamics of wet granules during fluidized-bed drying characterized with volumetric electrical capacitance tomography," Chemical Engineering Science. **75**, 220-234 (2012).

Rowe, P.N. and D.F. Everett, "Fluidized bed bubbles viewed by X-rays-Part II-bubble size and number when unrestrained three-dimensional growth occurs," Chemical Engineering Research and Design. **50**, 49-52 (1972).

Shen, L., F. Johnsson and B. Leckner, "Digital image analysis of hydrodynamics two-dimensional bubbling fluidized beds," Chemical Engineering Science. **59**, 2607-2617 (2004).

Toye, D., P. Marchot, M. Crine and G.L. Homer, "The use of large scale computer assisted tomography for the study of hydrodynamics," Chemical Engineering Science. **49**, 5271-5280 (1997).

van Lare, C.E.J., H.W. Piepers and D. Thoenes, "Investigation on bubble characteristics in a gas fluidized bed," Chemical Engineering Science. **52**, 829 - 841 (1997).

Warsito, W. and L.-. Fan, "Measurement of real-time flow structures in gas–liquid and gas–liquid–solid flow systems using electrical capacitance tomography (ECT)," Chemical Engineering Science. **56**, 6455-6462 (2001).

Weins, J. and T. Pugsley, "Tomographic imaging of a conical fluidized bed of dry pharmaceutical granule," Powder Technology. **169**, 49–59 (2006).

Werther, J., "Measurement techniques in fluidized beds," Powder Technology. **102**, 15-36 (1999).

Wormsbecker, M., T. Pugsley and H. Tanfara, "Interpretation of the hydrodynamic behaviour in a conical fluidized bed dryer," Chemical Engineering Science. **64**, 1739-1746 (2009).

Yang, W.Q. and L. Peng, "Image reconstruction algorithms for electrical capacitance tomography," Measurement Science and Technology. **14**, R1 - R13 (2003).